Bulletin of the Seismological Society of America, Vol. 106, No. 5, pp. 2345–2363, October 2016, doi: 10.1785/0120150215

Ⓔ

Modeling Earthquake Moment Magnitudes on Imbricate Reverse Faults from Paleoseismic Data: Fox Peak and Forest Creek Faults, South Island, New Zealand

by T. Stahl, M. C. Quigley, A. McGill, and M. S. Bebbington

Abstract Coeval rupture of imbricate reverse faults increases the moment magnitude (M_w) of the resulting earthquake. Detailed mapping and paleoseismic data can yield useful insights into the probability and M_w potential of multifault ruptures. We present a paleoseismic study of two active imbricate reverse faults, the Fox Peak and Forest Creek faults, in the central South Island of New Zealand. Both faults have recurrence intervals of ~3000 years, most recent events with overlapping age distributions, and sole into the same structure at depth. Surface and subsurface data indicate average single event displacements of ~2 m for the Fox Peak fault and 1 m for the Forest Creek fault. Monte Carlo simulations provide M_w estimates for a range of rupture scenarios (independent and combined), fault geometries, and coseismic displacements. The exponential fault-to-fault jump probability depends on the shortest distance between two faults, which is allowed to vary in the model based on regional hypocentral depths and the modeled fault geometries. Coulomb stress modeling is used to analyze stresses induced on the receiver fault plane, the Forest Creek fault, as a semiquantitative test of triggered rupture feasibility and to determine credible M_w distributions. The results suggest a maximum credible event (MCE) of $M_w \sim 7.5$–7.6 for listric geometries on the Fox Peak and Forest Creek faults. These estimates represent a 0.2–0.5 magnitude increase over most models, which show averages of $M_w \sim 7.1$–7.3 for rupture scenarios on planar faults. The Monte Carlo approach employed herein is an improvement over simple empirical relationships for estimating M_w for surface-rupturing earthquakes and MCEs for reverse-fault systems, because it provides realistic uncertainty estimates and can be readily applied to other fault systems around the world.

Online Material: Digital elevation model and sedimentation model of the trench 1 area, color trench logs with photomosaics, and detailed trench unit descriptions.

Introduction

Surface-rupturing earthquakes on reverse faults often involve many complex surface traces (Rubin, 1996) with master faults that extend into the subsurface. When multiple faults and/or fault segments rupture coevally, the total seismic moment can be significantly larger than if the hypocentral fault ruptures in isolation (Dolan *et al.*, 1995; Rubin, 1996; Beavan *et al.*, 2012; Elliott *et al.*, 2012; Oskin *et al.*, 2012). Recent earthquakes have shown that multifault earthquakes are more common than previously thought and can be attributed to either static or dynamic stress changes on nearby faults and fault segments (e.g., Oglesby *et al.*, 2003; Xu *et al.*, 2009; Elliott *et al.*, 2012; Oskin *et al.*, 2012; Field *et al.*, 2013; Fukuyama and Hao, 2013). Fault-to-fault triggering and segment jumping probabilities have recently begun to be implemented into seismic-hazard models (Shaw and Dieterich, 2007; Field and Page, 2011; Carpenter *et al.*, 2012; Parsons *et al.*, 2012; Field *et al.*, 2013).

Field data can help constrain fault parameters for modeling earthquake rupture scenario probabilities (e.g., Wesnousky, 2006; Biasi and Weldon, 2009; Parsons *et al.*, 2012; Hubbard *et al.*, 2014; DuRoss and Hylland, 2015). Rupture kinematics, fault geometry, frictional strength, pre-existing stress state, and coseismic slip distributions determine whether rupture will propagate onto another segment (Oglesby *et al.*, 2003; Lin and Stein, 2004; Elliott *et al.*, 2009; Schwartz *et al.*, 2012). Faults that do not intersect at the surface or that are blind are not typically involved in such analyses. In such cases, knowledge of whether the faults or segments are hard-linked (intersect at the surface or at depth, or have transfer faults) or soft-linked (have overlapping dimensions along strike or down dip) may play a critical role in whether rupture initiates on a secondary fault plane. For instance, the 2008 M_w 7.9 Wenchuan earthquake demonstrated that imbricate reverse faults soling into a single structure at depth can rupture in a single earthquake, probably due to dynamic stresses and favorable fault strength and geometry (Xu *et al.*, 2009; Densmore *et al.*, 2010; Zhu and Zhang, 2010; Fukuyama and Hao, 2013). The 1911 $M_w \sim 7.8$ Chon Kemin earthquake in the Tien Shan ruptured a wide zone of reverse and strike-slip fault segments of opposite vergence (Arrowsmith *et al.*, 2005). Using coulomb-linking stresses, Parsons *et al.* (2012) showed that imbricate ruptures in California involving two or more faults may be more likely than continuous rupture on a single fault. Hubbard *et al.* (2014) showed the potential for large magnitude earthquakes on imbricate reverse faults in the Transverse Ranges of California.

Two useful metrics in seismic-hazard analysis are the maximum moment magnitude (M_w) and maximum credible event (MCE) for fault sources. For surface-rupturing earthquakes on a fault over a defined recurrence interval (RI), maximum M_w can be determined from various scaling laws or direct calculation of the geologic seismic moment. The latter can be computed from field observations of fault length and average displacements (converted to subsurface values using regional seismologic datasets) and the shear modulus of the seismogenic crust. An estimation of MCE involves a subjective measure of the largest, time-independent earthquake that a fault or fault system is capable of producing (dePolo and Slemmons, 1990). Thus, in this article we consider that maximum M_w is the maximum likely magnitude for a source, and the MCE is the maximum possible earthquake for that source (e.g., Stirling *et al.*, 2002). Where two or more faults are being considered jointly, both metrics yield important information for seismic-hazard purposes.

In this study, we present a field and numerical approach to calculate maximum M_w distributions (hereafter M_w distribution) and the MCE of two imbricate reverse faults, the Fox Peak and Forest Creek faults, in the South Island of New Zealand. Paleoseismic and structural data reveal the potential for the two faults to rupture concurrently. M_w distributions are calculated via Monte Carlo simulations that incorporate field data. Coulomb failure stress modeling is conducted as a subjective measure of the feasibility of the specified rupture scenarios. This approach for estimating magnitudes for different rupture scenarios can be implemented into regional seismic-hazard models.

Study Site

The Fox Peak and Forest Creek faults are active back thrusts of the Pacific–Australian plate boundary in the central South Island of New Zealand (Fig. 1) (e.g., Upton *et al.*, 2004; Beavan *et al.*, 2007). Geodetically derived convergence rates at the plate boundary in New Zealand range from 30 to 50 mm yr^{-1} (Fig. 1) (Wallace *et al.*, 2007; DeMets *et al.*, 2010). Approximately 75% of this oblique convergence in the South Island is taken up on the Alpine fault, a 400-km-long, right-lateral oblique fault. In the Pacific plate of the central South Island, the remaining ~25% is distributed primarily onto reverse and thrust faults, such as the Fox Peak and Forest Creek faults (Fig. 1). Maximum net slip rates for the Fox Peak and Forest Creek faults are on the order of ~1.5 and 0.5 mm yr^{-1} at the surface, respectively (T. Stahl *et al.*, unpublished manuscript).

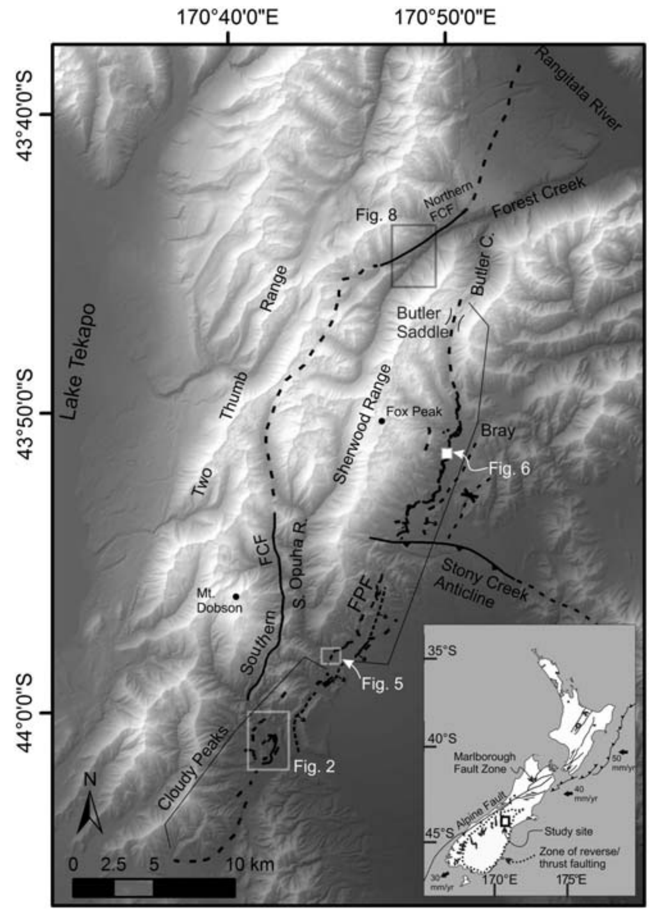

Figure 1. The study site within the simplified tectonic framework of New Zealand (inset) and simplified fault trace map (modified after Stahl *et al.*, unpublished manuscript). Fox Peak and Forest Creek fault traces and the locations of trench sites overlain on a 15 m digital elevation model (DEM): (1) Cloudy Peaks (Fig. 2), (2) South Opuha River area (Fig. 5), (3) Fox Peak ski field road area (Fig. 6), and (4) Forest Creek fault at Forest Creek (Fig. 8). The slip-rate-delineated Cloudy Peaks and Bray segments of the Fox Peak fault are labeled, along with those of the northern and southern segments of the Forest Creek fault. Dashed lines denote inferred fault traces and structures; black arrows along the Fox Peak fault are monocline axes.

Seismic and magnetotelluric surveys indicate that the Fox Peak and Forest Creek faults constitute a zone of back thrusting off the Alpine fault (Wannamaker *et al.*, 2002; Long *et al.*, 2003; Upton *et al.*, 2004; Beavan *et al.*, 2007), have surface traces that indicate ongoing activity through at least the latest Pleistocene, and are located in a region with relatively high Global Positioning System (GPS) uplift and contraction rates

(Beavan and Haines, 2001; Upton *et al.*, 2004; T. Stahl *et al.*, unpublished manuscript). Both faults are 30–40-km-long range-front structures that bound the Sherwood and Two Thumb ranges (Fig. 1). Seismic surveys (Long *et al.*, 2003) and field mapping (T. Stahl *et al.*, unpublished manuscript) indicate that the Fox Peak fault is listric in the shallow subsurface of the southern segment (see below) (Fig. 1). The Forest Creek fault switches its vergence along strike to accommodate uplift of the converging Sherwood and Two Thumb ranges (e.g., Jackson *et al.*, 1996) (Fig. 1).

Field mapping revealed three structural and geometric sections of the Fox Peak fault (Fig. 1) (T. Stahl *et al.*, unpublished manuscript). The along-strike slip-rate profile tapers toward a single segment boundary between the Bray and Cloudy Peaks segments (Fig. 1). The large displacement-surface rupture length ratios for each segment are consistent with full-length (i.e., multisegment) ruptures (T. Stahl *et al.*, unpublished manuscript).

Surface expression of the Forest Creek fault is found in the high relief areas of the Two Thumb range in hanging wall of the Fox Peak fault. In the north, an uphill facing scarp cuts across topography in a steep-sided valley for 4 km before continuing into Pleistocene glaciofluvial deposits as monoclinal folds (Cox and Barrell, 2007). In the south, the fault is defined by an uphill facing scarp and is exposed as a bedrock fault antithetic to the northern section (Upton *et al.*, 2004; T. Stahl *et al.*, unpublished manuscript).

Paleoseismology of the Fox Peak Fault

Four trenches were excavated (three on the Cloudy Peaks segment and one on the Bray segment) to determine the ages and displacements of past earthquakes on the Fox Peak fault. Trenches 1 and 2 were positioned across a crestal graben in the hinge zone of a Cloudy Peaks segment fault trace and anticline (location in Figs. 1 and 2). This location was chosen so as to maximize the probability of finding datable material and several earthquake horizons, which can be problematic in the reverse-faulting regimes of New Zealand's Southern Alps. Reconnaissance augering revealed fine-grained graben-fill sediments, some containing charcoal, in four locations. Additionally, satellite images and a Total Station microtopographic survey (Ⓔ Fig. S1, available in the electronic supplement to this article) reveal local topographic lows abutting normal fault scarps in a paleochannel, increasing the likelihood that ongoing slope wash processes could lead to small residence times of detrital wood/charcoal at the surface (i.e., ensuring that samples collected for radiocarbon dating within units are not vastly older than the deposits themselves). These faults were interpreted to be bending-moment normal faults related to the main reverse-fault trace; the ages of displacements should thus reflect those of the underlying reverse fault (e.g., McCalpin, 2009, p. 363). No strike-slip displacement could be detected from GPS mapping and surveying. The trenches were located in two separate grabens defined by oppositely dipping, bounding faults and

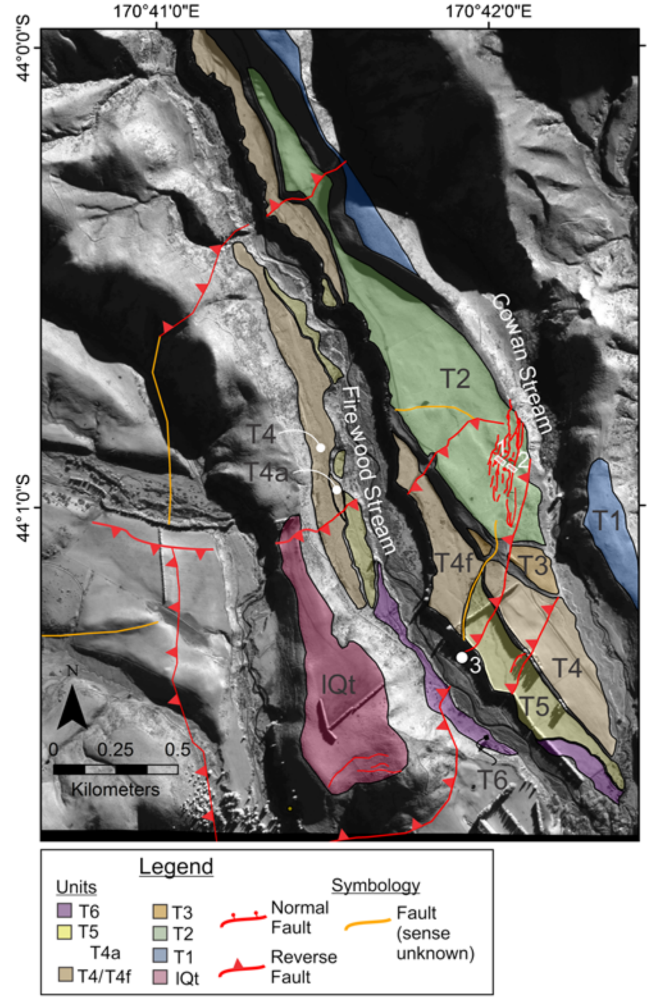

Figure 2. Near infrared GeoEye imagery and simplified neotectonic map of trench sites at the Cloudy Peaks segment of the Fox Peak fault (modified after Stahl *et al.*, unpublished manuscript). Fault traces with teeth are reverse faults (teeth on upthrown side). Traces without teeth are normal faults (without symbols due to density of the traces). Fault traces without symbols are unknown faults. T1–T6 denote terraces. LQt is a late Quaternary terrace of unknown age. Numbers 1, 2, and 3 are trench locations of corresponding number. The color version of this figure is available only in the electronic edition.

separated by a horst (Ⓔ Fig. S1) to account for the migration of the axial trace and bending-moment stresses through time (Gonzalez *et al.*, 2008).

Trench 3 was dug by hand across a scarp on the youngest displaced terrace at Cloudy Peaks. This location was chosen to obtain a potential single event displacement (SED) and most recent event (MRE) age on the main fault trace and to check the consistency of events with the bending-moment faults in trenches 1 and 2 (e.g., McCalpin, 2009, p. 363; Heddar *et al.*, 2013) (Fig. 2). The age of one event near the Cloudy Peaks–Bray segment boundary was inferred from the bounding ages of offset terraces (location in Fig. 1).

Trench 4 was located across a fault trace adjacent to the Fox's Peak ski field road on the Bray segment (location in Fig. 1). At this location, a single trace northeast of the trench

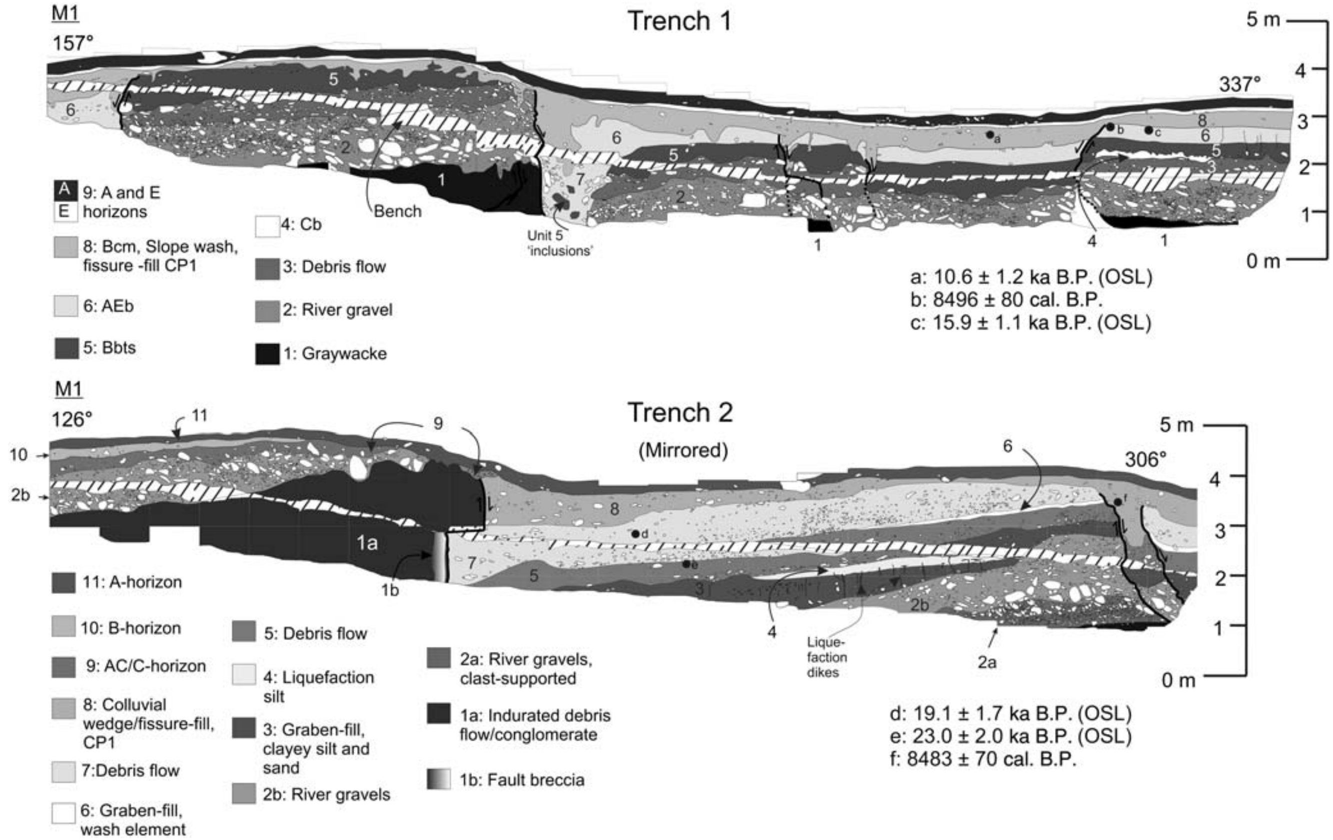

Figure 3. Trenches 1 and 2. Note that the faults bounding paleo-free faces are drawn as solid (shown in black) to the stratigraphic level that they offset units on the hanging wall; this does not imply that all units in contact with the fault on the paleo-free face have been offset by that fault. In trench 1, unit 8 has in-filled fissures during deposition—it is the oldest unfaulted unit exposed in the trench. Also note the dashed contact between unit 6 (loess) and unit 7 (fissure fill composed mainly of unit 6) near the fault with the greatest amount of offset and dilation in trench 1. Diagonal hatching denotes a bench in the trench wall. Rectangular edges around the trench wall are the limits of photos used to make the photomosaic.

site splays into three separate traces as it crosses a paleochannel. Surveying of the paleochannel and the surfaces to either side of the trench site revealed that (1) changes in elevation of the two surfaces are ±1 m and attributable to natural undulations or radial slope of the surface and (2) the paleochannel is offset the same amount as the surface to the south (summed across the traces). Therefore, we determined that there is no resolvable difference between the surface on either side of the paleochannel, and any difference in net slip is likely due to a change in fault dip, expressed as splaying of surface traces, as the fault approaches the free face of the stream. Similar patterns of changing fault scarp morphology and dip are observed further along the Fox Peak fault (T. Stahl *et al.*, unpublished manuscript).

The findings in each of the trenches are discussed in detail below. Ⓔ In all instances, please refer to the electronic supplement for full-size color versions of the trench logs and photomosaics.

Cloudy Peaks Segment

Trench 1. Excavation revealed five faults in trench 1 with individual vertical displacements ranging from ~0.02 to 1.42 ± 0.10 m (Figs. 2 and 3). Trench stratigraphy consisted of a Torlesse graywacke bedrock strath (unit 1) underlying an ~1-m-thick bed of imbricated fluvial gravels (unit 2). As expected, measurements of imbrication indicated a flow direction for the paleochannel parallel to that of the Firewood and Cowan streams (Fig. 2). A buried soil profile (units 4–6) is developed in loess on top of a matrix-supported debris-flow deposit (unit 3) that consists of elongate, flat-lying clasts in a silt matrix. Units 1–6 are offset and down-dropped into fissures across the graben. Unit 7 is composed entirely of collapsed unit 6. A slope wash deposit composed primarily of silt (unit 8), drapes minor fault scarps, and further in-fills near vertical voids left by fissuring, indicating that it was deposited soon after faulting. Unit descriptions are summarized in Ⓔ Table S1. The sequence of deposition/faulting is as follows:

1. beveling of bedrock strath (unit 1) and subsequent fluvial incision in the Firewood stream causing abandonment of fluvial gravels (unit 2);
2. deposition of debris flow (unit 3) during abandonment or from flooding event in nearby drainage (Cowan stream);
3. accumulation of loess (units 4 and 5), presumably sometime during the last glacial maximum (LGM) or earlier;

Table 1
Infrared Stimulated Luminescence (IRSL) Results from Trenches 1, 2, and 4

Sample Number*	Deposit	dD_c/dt (Gy/ka)†	Water Content (%)	K (%)	U (ppm) from ^{234}Th	U (ppm) from ^{226}Ra, ^{214}Pb, ^{214}Bi	U (ppm) from ^{210}Pb	Th (ppm) from ^{208}Tl, ^{212}Pb, ^{228}Ac	a-Value	D_e (Gy)‡	dD/dt (Gy/ka)§	Age (ka)
WLL944, *sample a*	Trench 1, unit 8	0.2153 ± 0.0108	30.88	1.97 ± 0.04	3.46 ± 0.28	3.37 ± 0.17	2.95 ± 0.22	10.23 ± 0.14	0.08 ± 0.03	34.33 ± 1.33	3.25 ± 0.35	10.6 ± 1.2
WLL945, sample d	Trench 2, unit 7	0.1948 ± 0.0097	26.98	1.97 ± 0.04	1.85 ± 0.04	3.16 ± 0.16	3.11 ± 0.21	12.09 ± 0.14	0.07 ± 0.01	70.09 ± 4.20	3.66 ± 0.25	19.1 ± 1.7
WLL947, *sample c*	Trench 1, unit 6	0.2153 ± 0.0108	21.85	1.67 ± 0.04	3.32 ± 0.34	2.81 ± 0.20	3.20 ± 0.27	11.74 ± 0.16	0.07 ± 0.01	58.77 ± 2.04	3.69 ± 0.22	15.9 ± 1.1
WLL948, *sample e*	Trench 2, unit 5	0.2059 ± 0.0103	31.13	1.75 ± 0.04	3.33 ± 0.29	3.39 ± 0.18	3.99 ± 0.25	13.01 ± 0.16	0.07 ± 0.003	83.46 ± 4.46	3.63 ± 0.24	23.0 ± 2.0
WLL1000, *sample b*	Trench 4, unit 3	0.1978 ± 0.0099	23.5	2.15 ± 0.04	3.39 ± 0.26	3.29 ± 0.16	3.43 ± 0.22	13.35 ± 0.15	0.06 ± 0.02	67.57 ± 6.50	4.13 ± 0.32	16.4 ± 2.0

Italicized sample IDs in the first column refer to notation in trench logs.
*Sample preparation and measurements performed at School of Earth Sciences, Victoria University of Wellington, Wellington, New Zealand.
†Contribution of cosmic radiation to the total dose rate.
‡Equivalent dose.
§Dose rate.

4. soil development within loess with top of unit 6 (AEb horizon) as paleosurface;
5. faulting event CP1: simultaneous offset of units 1–6 on faults 1–5; discrete blocks of previously developed soil down-dropped into major fissure; fluvial gravels form collapse-fabric on fissure margins;
6. slope wash (unit 8) from surrounding topography (scarps and channel margins) in-fills remaining voids formed by faulting and drapes scarps within graben. The near vertical contact between unit 8 and underlying units is a result of fissure-infilling and redeposition of primarily unit 5/6 (redeposited unit 5/6 is mapped as unit 8); and
7. further soil development with formation of modern A and E horizons, translocation of fines to unit 8 and partial welding of the buried soil (units 4–6).

One radiocarbon and two infrared stimulated luminescence (IRSL) samples were taken to constrain the age of faulting. All radiocarbon samples were analyzed on an accelerator mass spectrometer at Rafter Radiocarbon Laboratory in Lower Hutt, New Zealand; calibrations were performed using the southern hemisphere atmospheric correction of McCormac *et al.* (2004). As the timing of faulting lies between the ages of the stable surface formed by unit 6 and that of postfaulting deposition of unit 8, one IRSL sample was taken from each unit. Unit 6 has a luminescence age of 15.9 ± 1.1 ka (Fig. 3, sample c; Table 1), which is consistent with the timing of late to post-LGM loess deposition elsewhere in the South Island (e.g., Alloway *et al.*, 2007). An age of 8496 ± 80 cal. B.P. (2σ) was obtained for detrital charcoal at the top of unit 6 (Fig. 3, sample b), near or within the indistinct contact with unit 8 and immediately adjacent to a fault (Fig. 3). We consider the IRSL age of 15.9 ± 1.1 ka to best represent the depositional age of unit 6 and hypothesize that the charcoal was integrated into unit 6 from overlying unit 8 by soil mixing processes. A luminescence age of 10.6 ± 1.2 ka was obtained for unit 8 (Fig. 3, sample a; Table 1) which is closer to the radiocarbon age of sample (b) obtained stratigraphically below it, supporting our hypothesis that unit 8 is of early Holocene age. The small difference may be due to incomplete bleaching of the source material for IRSL sample (a) during relatively short transport within the local basin (e.g., Ⓔ Fig. S1). We thus assign an age of 8496 ± 80 yr B.P. for this earthquake identified as CP1.

Trench 2. Excavation revealed three faults with vertical displacements of the uppermost strata ranging from 1.3 ± 0.20 to 0.38 ± 0.10 m (Figs. 2 and 3). The style of faulting and sedimentation is markedly different than in trench 1 that is located 40 m to the northwest on the same terrace. A strongly indurated breccia with clasts of Torlesse graywacke sandstone (unit 1a) forms the strath in this location, which is overlain by fluvial gravels (units 2a and 2b). Unit 1a is backtilted on the footwall of the principal fault but not apparent elsewhere in either trench 1 or 2. A sliver of indistinct bedrock (either Torlesse graywacke bedrock or unit 1a breccia) is present on the hanging wall. Trench flooding and a limited depth of excavation prevented identification of the basal unit on the hanging wall. It is likely that unit 1a is a localized deposit of limited lateral extent from an earlier phase of faulting or from landsliding at the old river margin. Unit 1b, fault breccia, is only evident along the main fault zone. It is likely to have been in-faulted along unit 1a prior to the initiation of normal faulting in the crestal graben, further evidenced by a small gouge zone smeared along the modern fault plane. Unit 3, overlying the fluvial gravels (unit 2), is a silt loam with manganese nodules and iron-staining, indicating sustained saturation during a period of prolonged soil development, probably in a pre-existing topographic low. Liquefaction dikes (Fig. 3), sourced from fluvial silts of unit 2b, crosscut unit 3 and have created a silt deposit (unit 4), interpreted as a sandblow, which drapes the top of unit 3. Some liquefaction dikes crosscut and reintruded unit 4. A debris-flow unit with flat-lying, irregular clasts at its base (unit 5) overlies unit 4. Unit 6, a clayey silt and sand, thins toward the southeast and is overlain by a second debris flow unit (unit 7). A colluvial wedge (unit 8) overlies unit 7 and has the modern A horizon (unit 11) developed directly on to it on the hanging wall. On the footwall, the A horizon overlies B (unit 10) and C (unit 9) horizons. At the scarp interface, the A horizon is developed directly on the C horizon. Unit descriptions are summarized in Ⓔ Table S2.

The hanging wall stratigraphy shows evidence of progressive faulting via up-section flattening of dips and thickening of deposits toward the principal fault. The sequence of deposition/faulting is as follows:

1. deposition and induration of unit 1a in an alluvial environment prior to incision down to the base level of paleochannel;
2. faulting creates unit 1b;
3. river incision and deposition of units 2a and 2b (unit 2) prior to abandonment of terrace;
4. earthquake (CP3) on principal fault offsets existing stratigraphy and tilt units 2a and 2b (unit 2) on hanging and footwalls;
5. fine sediment (unit 3) fills in fault-bounded low created by CP3. Deposit thickens toward scarp;
6. rudimentary soil development in unit 3;
7. earthquake shaking from faulting event CP2 induces liquefaction and deposition of unit 4; dikes reactivated during subsequent earthquakes or aftershocks; further hanging and footwall tilting of units 1a and 2a,b; hanging wall tilting of unit 3;
8. deposition of unit 5 debris (hyperconcentrated) flow, infilling new fault-bounded basin and thickening toward principal fault scarp;
9. slope wash sedimentation (unit 6) thickens toward the axis of graben;
10. possible earthquake: minor initial tilting of units 5 and 6 and deposition of debris flow (unit 7);
11. earthquake (CP1), tilting of units 5–7, further tilting of underlying strata. Offset of units across two secondary faults at the northwestern end of the trench;
12. deposition of colluvial wedge (unit 8), thickening toward principal fault scarp and in-filling fissure between secondary faults (where it is present as collapsed unit 7);
13. modern soil development (units 9–11).

A radiocarbon and two IRSL samples were taken to constrain the timing of the MRE (CP1) and older events. The timing of the MRE was constrained by charcoal detritus found within the colluvial wedge deposit (unit 8: Fig. 3, sample f). The charcoal returned an age of 8483 ± 70 cal. B.P., which is within error with the radiocarbon sample taken from trench 1 (Fig. 3, sample b). It represents a probable age of MRE faulting (at this location) that affected both grabens in this zone of normal faulting.

A luminescence age of 19.1 ± 1.7 ka for the underlying debris-flow deposit (unit 7: Fig. 3, sample d) is consistent with the expected chronologic and stratigraphic ordering (Table 1). It is peculiar that there is no evidence of a soil having developed on unit 7, given the 10 ka interval between its deposition and that of unit 8. Periodic renewal and deposition of fines from aeolian and wash deposition in the pre-existing low may have outpaced pedogenesis, in which case the age of 19.1 ± 1.7 ka may represent an average for unit 7 (a maximum age for its top and a minimum for its base). This model of deposition would also explain the apparent lack of late LGM loess in trench 2 that was observed in trench 1, as it would have been incorporated into unit 7.

A luminescence age of 23.0 ± 2.0 ka was obtained for unit 5 (Fig. 3, sample e; Table 1). This represents a minimum age for the remainder of the units and faulting observed in trench 2. Therefore, a possible earthquake, apparent only in a dip increase (i.e., rollover) from unit 7 to unit 6 has an age between 19.1 ± 1.7 and 23.0 ± 2.0 ka.

Trench 3. Excavation across a scarp on the lowest offset terrace at Cloudy Peaks (dated to $3.7^{+3.5}_{-2}$ ka B.P., T. Stahl *et al.*, unpublished manuscript) revealed evidence for 1.0 ± 0.2 m of vertical offset across the 7 m length of the trench (Fig. 4). Vertical offset at the fault is less than 0.5 m; a large percentage of the total deformation is accommodated by coseismic folding accompanying faulting (e.g., Gold *et al.*, 2006; Amos *et al.*, 2011). The net slip at this location, determined from a survey transect over the length of the terrace, is ~1.8 m (T. Stahl *et al.*, unpublished manuscript). Fluvial gravels, silt, and sand (units 1 and 2) are overlain by finer and more uniform overbank silts (unit 3). Unit 3 is thickest in a small sag on the hanging wall, which is interpreted as a tectonic feature. This suggests that faulting occurred while the terrace was active, trapping additional fines, or that flooding (and further silt deposition in the sag) occurred soon after faulting. On the footwall of the fault, a thickened B horizon (unit 3) indicates significant cumulic input from slope wash that has outpaced soil development since faulting. The source of at least some of this material is unit 3 on the hanging wall, which thins toward the scarp due to enhanced erosion (Fig. 4). An AC horizon (unit 5) grades laterally into

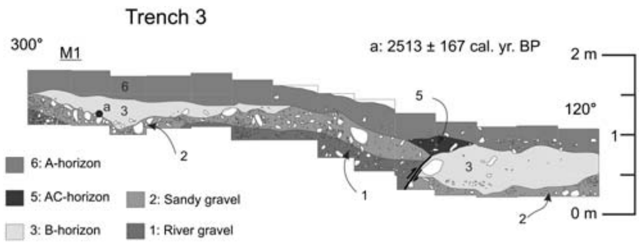

Figure 4. Trench 3. Rectangular edges around the trench wall are the limits of photos used to make the photomosaic.

unit 3 on the hanging wall and overlies the fault. The modern A horizon (unit 6) is noticeably stonier at its base on the footwall and grades laterally into unit 5 near the fault. Unit descriptions are summarized in Ⓔ Table S3. The sequence of deposition/faulting is as follows:

- aggradation of fluvial gravel, silt, and sand (units 1 and 2); possible initial deposition of overbank silts (unit 3);
- terrace abandonment;
- faulting and folding of units 1–3 (CP3); further input of fines into hanging wall syncline via flooding;
- scarp erosion and pedogenesis form thickened B horizon on hanging wall, AC horizon (unit 5), and rough stone line at base of modern A horizon.

Charcoal at the unit 2/3 contact on the hanging wall yielded an age of 2513 ± 167 cal. B.P. (Fig. 4, sample a). This represents a minimum age for the abandonment of the terrace and a maximum age for the earthquake that produced the fault scarp. There is no minimum age constraint on the timing of faulting; however, the degree of soil development in the footwall (i.e., thickened B horizon and crude AC horizon) probably requires at least ~1 ka to develop (e.g., Tonkin and Basher, 1990). This skews the preferred age for the MRE on this trace toward that of a maximum 2513 ± 167 yr B.P., with a decreasing likelihood of a younger age toward ~1 ka (see the Synthesis of Paleoseismic Data for the Fox Peak and Forest Creek Faults section). Upton and Osterberg (2007) attributed mass-movement deposits in Lake Tekapo (~15 km to the west, Fig. 1), dated to 1720 ± 344 and 2810 ± 562 yr B.P., to earthquakes on nearby faults. These ages are generally consistent with the MRE at Cloudy Peaks, but assumptions in determining the ages of the mass-movement deposits (i.e., based on sedimentation rates) and a wide range of seismic sources makes their correlation with a Fox Peak fault earthquake difficult.

We note that this MRE is not apparent in trenches 1 and 2, confirming observations from elsewhere that bending-moment faults are not active in all earthquakes on the master reverse-fault trace (McCalpin, 2009, p. 363; Heddar *et al.*, 2013).

Cloudy Peaks–Bray Segment Boundary

The segment boundary between the Cloudy Peaks and Bray segments is marked by a decrease in along-strike slip-rate profile, an inferred bedrock fault, and the southern termination

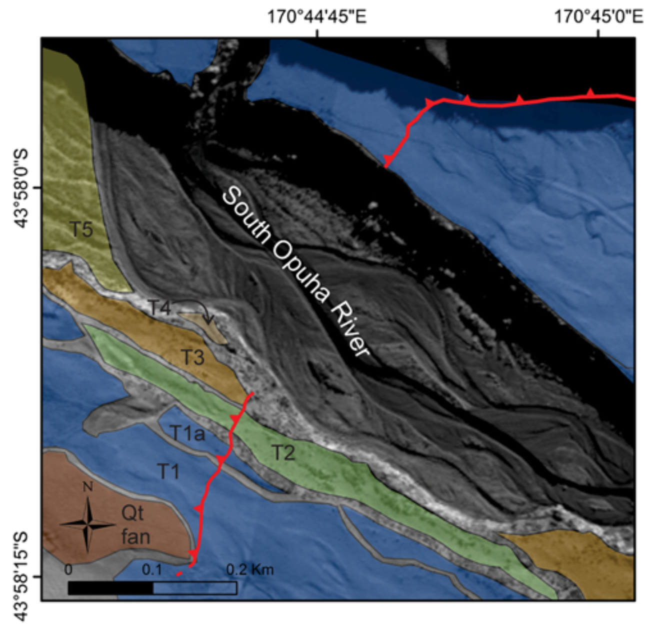

Figure 5. Simplified geomorphic map of the Fox Peak fault at the South Opuha River terraces. The throws across the fault on T1, T2, and T3 are all the same within error. T4 and T5 are not offset by the fault, limiting the age of faulting to lie between the ages of abandonment for T3 and T5. These ages, derived from Schmidt hammer exposure-age dating (Stahl *et al.*, 2013) are $6.5^{+2.2}_{-1.8}$ and $4.2^{+1.7}_{-1.3}$, respectively (T. Stahl *et al.*, unpublished manuscript). The color version of this figure is available only in the electronic edition.

of the Sherwood range (T. Stahl *et al.*, unpublished manuscript). Here, the South Opuha River emerges from the ranges to the west and has abandoned terraces of less than ~18–14 ka age. There is evidence of only one event on the main trace of the Fox Peak fault at the South Opuha River (Fig. 5). Displaced terraces (T1, T2, and T3) are all offset by the same amount (~0.85 m net slip). There is no evidence that T4 is offset at the fault. This constrains the timing of the earthquake to lie between the abandonment of T3 and T4. Because no ages could be obtained from T4, the age of T5 is used as a minimum age constraint. Schmidt hammer exposure-age dating (see Stahl *et al.*, 2013, for a full review of this methodology), a calibrated age-dating technique for quantifying the time a surface clast has spent weathering at the terrace surface, suggests that the ages of T3 and T5 are $6.5.^{+2.2}_{-1.8}$ and $4.2.^{+1.7}_{-1.3}$, respectively (T. Stahl *et al.*, unpublished manuscript). Thus, the best estimate for the age of this earthquake is between ~4.2 and 6.5 ka. We note that the MRE at Cloudy Peaks is not evident at the South Opuha River, which may indicate either a segmented rupture spanning only the length of the Cloudy Peaks segment or a lack of surface expression of the MRE on the terraces on the south side of the South Opuha River (Fig. 5). Although the former is possible, the latter interpretation of a multisegment rupture is preferred, given the evidence for progressive flexural slip folding on the north side of the river and the large SED estimates for the Cloudy Peaks segment. The latter imply > 30 km rupture lengths (using relationships of Wells and Coppersmith, 1994; Wesnousky, 2008), compared

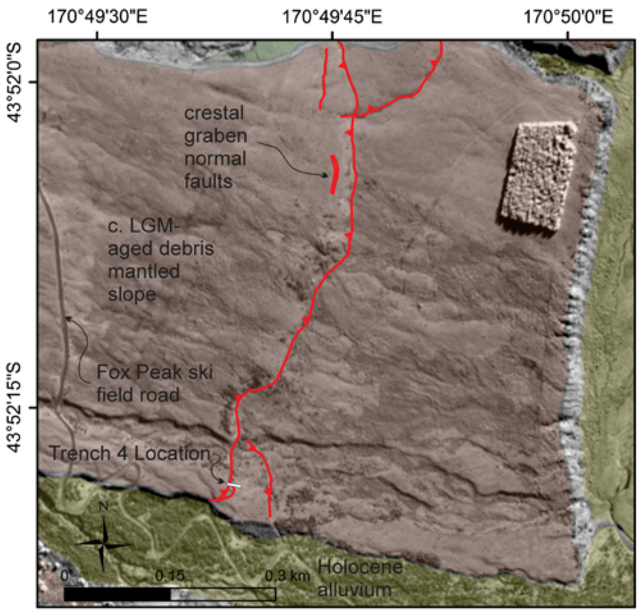

Figure 6. Near infrared GeoEye imagery and simplified neotectonic map of trench 4 site at the Fox Peak ski field road. The color version of this figure is available only in the electronic edition.

to actual surface rupture lengths of 8.5–16 km for the segments (T. Stahl *et al.*, unpublished manuscript).

Bray Segment

The northern Bray segment of the Fox Peak fault is marked by a semicontinuous, west-dipping range front fault. Where present as a single trace on post-LGM and LGM surfaces, the scarp is over 15 m high with net slip rates over $\sim 1\ \mathrm{mm\,yr^{-1}}$ (T. Stahl *et al.*, unpublished manuscript). Trench 4 was located on a post-LGM debris-mantled slope where slip rates were determined to be near a maximum for the segment.

Trench 4. Excavation revealed that the north and south walls of trench 4 had marked differences in the appearance of deposits and faults (Figs. 6 and 7). Accordingly, both walls were logged. The oldest unit in both cases is a poorly sorted, clast-supported gravel with sand lenses and a sandy matrix (unit 1). This unit forms the base of the debris-mantled slope, which likely formed periglacially from the catchment near Fox Peak. Alternations between debris flow and small channel deposition occurred before abandonment of the surface.

North Wall and Depositional History. Four moderately to steeply dipping fault splays with a cumulative vertical displacement significantly less than the modern scarp height were observed on the north wall (Fig. 7). This suggests a combined faulting–folding mechanism leading to the modern scarp dimensions, or that the master fault is concealed. On the footwall of the visible faults, matrix-supported, subrounded gravel (unit 2) underlies channel deposits consisting of silts, sands, and gravel lenses (unit 3). A chaotically bedded, subrounded-to-angular debris flow (unit 4) overlies these deposits and is cut off by colluvial wedge deposits toward the fault scarp. Units 1–4 are consistent with periglacial–alluvial deposition of the debris-mantled slope and predate all evidence of faulting. The slope of the surface, height of the fault scarp, and the lack of cohesion in the gravels limited the extent to which these units could be exposed on the hanging wall. However, units 1–4 appear in a small exposure at the top of the trench (Ⓔ Fig. S5: north wall of trench 4).

Deposition after abandonment of the surface is dominated by fault-derived colluvium. An inferred, crescent-shaped colluvial wedge (unit 5) is marked at its base by a line of large boulders and bordered by other units at its edges. Unit 5 overlies units 2 and 3 but abuts unit 4 at a similar stratigraphic level. Together with the lack of apparent soil development and fine material in the wedge, this implies that deposition of this unit occurred soon after or during abandonment of the surface. A second colluvial wedge (unit 6) is again marked at its base by a layer of coarse boulders, here entrained in an orange, silty clay matrix. Units 8a and 8b constitute different facies of fissure fill and colluvium from the MRE. Unit 8a is a free-face collapse deposit (reworked unit 1). Unit 8b is a matrix-supported gravel deposit that infills an ~0.5-m-wide fissure between units 1 and 6 and forms a downslope thinning unit, which consists of remobilized unit 4. The scarp and all units are overlain by a rocky AC horizon (unit 9). Unit descriptions are summarized in Ⓔ Table S4. The sequence of deposition/faulting is as follows:

- periglacial deposition of debris flow/alluvial fan gravels, sand and silt (units 1–4);
- abandonment of till sheet surface;
- faulting (Br1) soon after surface abandonment and deposition of colluvial wedge 1 (unit 5);
- stabilization of slope as fines accumulates at surface (soil formation or loess?);
- faulting (Br2) and incorporation of fines of (iv) into colluvial wedge 2 (unit 6);
- stabilization of slope and soil formation;
- faulting (Br3): in-filling of fissure on scarp (units 8a and 8b) and downslope mobilization of unit 4 (unit 8b). It is likely that the small offsets and folding observed in the trench on all four faults occurred during this MRE;
- formation of AC Horizon over sedimentary package.

A radiocarbon and IRSL sample were taken from the north wall of trench 4. Detrital charcoal was found within unit 8b downslope of the 8a fissure-fill facies (Fig. 7, sample a). This provides a maximum age for the MRE of 3479 ± 79 cal. B.P. Given the degree of weathering of unit 8 and the AC horizon developed on top of it, the preferred age for the deposit is skewed toward the maximum bound of this age.

A luminescence age of 16.4 ± 2.0 ka was obtained for unit 3 (sample b, Table 1). No other datable material was found in the remainder of the trench. The age of unit 3 provides a maximum age for Br1 and Br2 and establishes an approximate age of the till sheet to being near the end of the LGM in New Zealand (e.g., Alloway *et al.*, 2007).

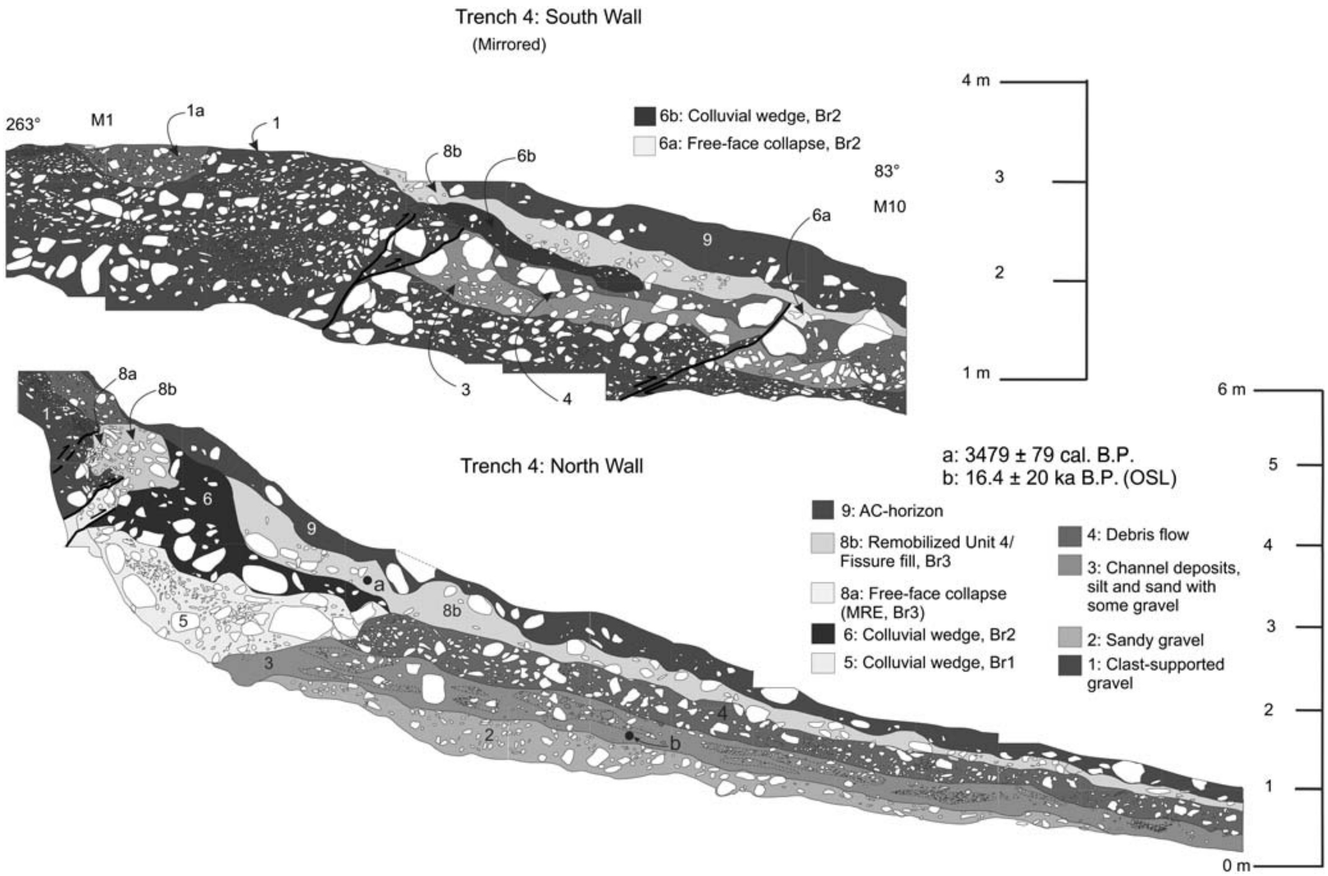

Figure 7. Trench 4. Rectangular edges around the trench wall are the limits of photos used to make the photomosaic.

Trench 4 South Wall. Excavation revealed evidence for two moderately dipping fault zones that offset units 1–4 (Fig. 7). Unit 2 on the north wall is not distinguishable here, and the well-developed channel's deposits of unit 3 are not present. This may indicate that a pre-existing relief on the south side of the trench site (e.g., a fault scarp) directed flow and channel deposits toward the current footwall of the north wall. This topography would predate Br1 on the north wall. A thin colluvial wedge (units 6a and 6b) overlies the faulted strata, which is correlated with unit 6 on the north wall, due to similar sedimentology and weathering. Unit 8b, which immediately postdates the MRE, overlies the colluvial wedge unit 6, and both are undeformed. Thus, the faults on the south wall were only active during Br2. No datable material was found to constrain the age of this event. A cumulative net slip of 2.2 ± 0.3 m was calculated across the two faults. This is likely to be a minimum estimate for the true SED at this site; displacement must have occurred on obscured faults under the north wall in Br2, and no SED was measured for the trace just downslope of the trench site.

Single Event Displacements and Recurrence Interval

The best estimate of an average surface SED from trenching both segments is ~2 m (SED from trench 4 on the Bray segment and net slip from trench 3 location on the Cloudy Peaks segment), which agrees well with empirical predictions from the Wesnousky (2008) length scaling relations for reverse faults (e.g., 37-km rupture length [T. Stahl *et al.*, unpublished manuscript] yields a 2.2-m-average geologic slip). As an internal check on this estimate, we compare RIs derived using this SED versus the RI observed in trenches. Using an average surface slip rate (i.e., derived using all measured net slips, fault geometries, and slip rates over the length of the fault) of $\sim 0.8\ \mathrm{mm\,yr^{-1}}$ (T. Stahl *et al.*, unpublished manuscript) and a 2 m SED, an average RI of ~2500 years is calculated. Obtaining an RI from earthquakes recorded in trenches is more difficult to determine. The north wall of trench 4 provides evidence for 3–4 events over ~16 ka, suggesting an average RI of 4000–5300 years. This relatively long period provides upper bounds for the RI, given that some events may have ruptured only through the frontal scarp that was not trenched at this location (Fig. 6). The MRE at Cloudy Peaks (~1000–2500 yr B.P.) and at Fox Peak ski field road (~1000–3500 yr B.P.), an event inferred at the South Opuha River terraces (~4200–6500 yr B.P.), and the antepenultimate event observed in the bending-moment fault trenches (trenches 1 and 2, best estimate of 8490 ± 87 yr B.P. using the combined calendar ages from radiocarbon samples) suggest an actual RI for the Fox Peak fault on the order of 3500 years. Thus, while subject to considerable uncertainty, an average SED of

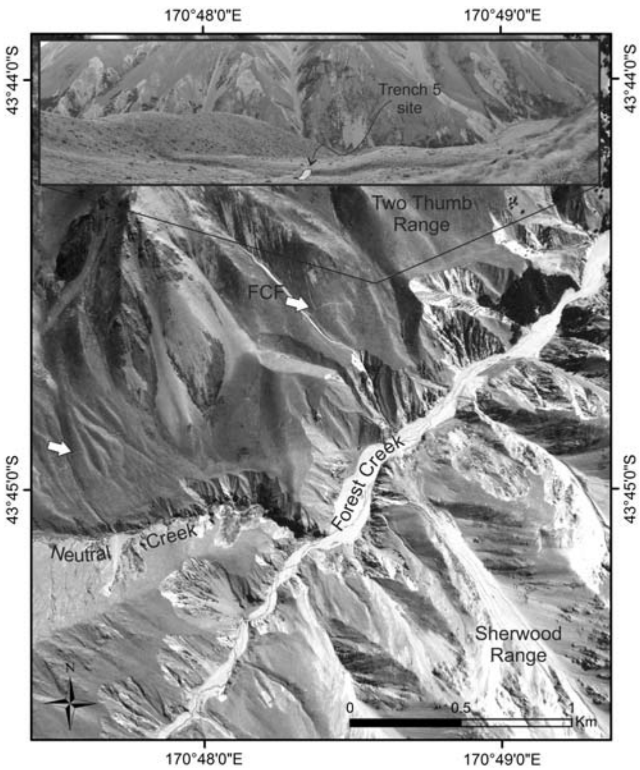

Figure 8. Historical aerial photograph and field photograph (inset) of the Forest Creek fault at trench 5 site.

2 m and RI of ∼2500–3500 years represent our best estimates from the paleoseismic data.

Paleoseismology of the Forest Creek Fault

Forest Creek Scarp: Trench 5

A hand-dug trench was excavated across the scarp shown in Figure 8. The location was chosen to coincide with the edge of a scarp-impounded pond. Excavation revealed two fault splays separating primarily graben-fill sediments on the hanging wall from slope colluvium on the footwall (unit 1) (Fig. 9). On the footwall, unit 1 is overlain by A and E horizons (units 9 and 10). The A horizon thickens, becomes more clay-rich, and contains peat horizons on the hanging wall (unit 10). Units 2–5 are dragged along the principal fault plane and offset by a more gently dipping intersecting fault. Unit 3 is composed of dark-colored clay and contains charcoal fragments, suggesting it is a buried A or O horizon. Units 2, 4, and 5 are clayey silts and silty clays that are interpreted to be older graben-fill sediments. Onlapping the vertical units 2–5 are horizontally bedded, modern graben-fill sediments (units 6 and 7), which are drag folded at the gently dipping fault. A matrix-supported gravel (unit 8) derived from unit 1 and the footwall soil horizons is perched between unit 1 and units 6 and 7. This is interpreted to be a colluvial wedge/fissure-fill deposit (unit 8) that formed following the MRE. Unit descriptions are summarized in Ⓔ Table S5. The sequence of deposition and faulting is as follows:

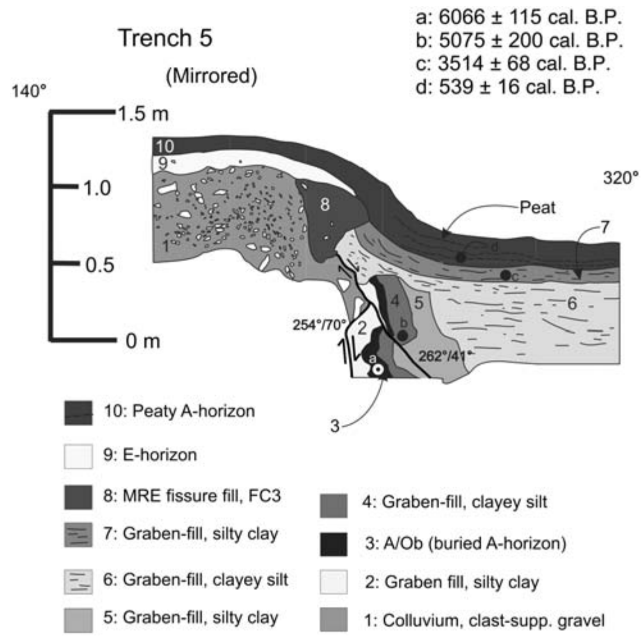

Figure 9. Trench 5. See the Paleoseismology of the Forest Creek Fault section for discussion.

- deposition of colluvium (unit 1) on steep slope;
- faulting (FC1) and offset of unit 1;
- postseismic accumulation of fines (unit 2 and underlying strata) against scarp;
- organic A or O horizon (unit 3) develops at pond edge as slope stabilizes;
- second accumulation of fines (units 4 and 5) and burial of unit 3, possibly in a flood behind FC1 scarp;
- faulting (FC2) and drag-folding of units 2–5 into a vertical orientation;
- accumulation of fines behind scarp (units 6 and 7) and near total filling of graben;
- faulting (FC3), minor offset of units 2–5, and drag folding of units 6 and 7; fissure/colluvial wedge develops above fault tip in region of extension;
- scarp is defeated by modern drainage, and pond level lowers, leaving modern A and peaty O horizons (unit 10) to develop in trench area, thickest on hanging wall.

Four radiocarbon samples were taken from trench 5 (Fig. 9, samples a–d). Charcoal in unit 3 (actual sample (a) location located on trench floor, Ⓔ Fig. S7) yielded an age of 6066 ± 115 cal. B.P. and provides a maximum age for unit 3. Detrital charcoal in unit 4 (sample b) returned an age of 5075 ± 200 cal. B.P. and provides a minimum age of unit 3. Therefore, the antepenultimate earthquake (FC1) occurred before 5570 ± 611 cal. B.P. (i.e., sometime before the deposition of unit 3). Charcoal in unit 7 (sample c) yielded an age of 3514 ± 68 yr B.P., which is a minimum age for unit 6. Because FC2 occurred between deposition of units 5 and 6, FC2 occurred between ∼5.5 and 3.5 ka, probably closer to 5.5 ka. Earthquake FC3 occurred between deposition of unit 7 and modern soil formation. Peat in the lower portion

Table 2
Synthesis of Paleoseismic Event Ages and Correlations

Fault/Segment/ Location	Trench Number/ Age Constraint	Local Event Name	Age Range	Observational Constraints	Preferred Age Distribution
Fox Peak–Cloudy Peaks	1	CP1	8496 ± 80	Corresponds to age of CP1 in trench 2; slightly younger than IRSL age for unit 8 (10.6 ± 1.2 ka)	Normal: 8490 ± 500 (2σ)
Fox Peak–Cloudy Peaks	2	CP1	8483 ± 70	Corresponds to age of CP1 in trench 1	Normal: 8490 ± 500 (2σ)
Fox Peak–Cloudy Peaks	3	CP3	<2513 ± 167	Maximum age is likely to be near true age of deposit, based on soil development	Exponential: Maximum: 2513 ± 167 Lower cutoff: 0
Fox Peak–South Opuha River	Terrace ages	SO2	$4.2._{-1.3}^{+1.7}$ to $6.5._{-1.8}^{+2.2}$	None	Normal: 5350 ± 1150
Fox Peak–Bray	4	Br3	<3479 ± 79	Maximum age is likely to be near true age of deposit, based on soil development	Exponential: Maximum: 3479 ± 79 Lower cutoff: 0
Forest Creek-Northern	5	FC1	>5570 ± 611	None	None
		FC2	3514 ± 68 to 5570 ± 611	Closer to 5570 ± 611 based on thickness and time required for deposition of unit 6	Bounded exponential: Maximum I: 5570 ± 611 Maximum II: 3514 ± 68
		FC3	539 ± 16 to 3514 ± 68	Closer to 539 ± 16 based on preservation of discrete peat bands within unit 10	Bounded exponential: Maximum I: 539 ± 16 Maximum II: 3514 ± 68

of the modern A/O horizon (sample d) returned an age of 539 ± 16 cal. B.P. Thus, FC3 (MRE) occurred between 3.5 and 0.5 ka, and probably closer to 0.5 ka, given the preservation of discrete peat bands within the A/O horizon (unit 10: Fig. 9).

Single Event Displacement and Recurrence Interval

An SED is difficult to calculate from the available information on the Forest Creek fault. The MRE produced only a few centimeters of throw on discrete faults in trench 5 (Fig. 9). However, if it is assumed that the accommodation space for the unit 8 fissure was created in FC3, and some of the displacement was distributed onto the steeply dipping fault at depth, then throw was on the order of ~0.6 m (separation of unit 7 on the hanging wall from the top of unit 1 on the footwall). To produce the drag folding of units 2–5 in two earthquakes, total displacement would have to be a minimum of 1.4 m (separation of base of trench to top of unit 1). Units 2–5 are drag-folded into the fault and dip vertically into the trench floor (Ⓔ Fig. S7), indicating that throw in the penultimate event (and an SED) would be greater than 0.8 m. We therefore estimate an SED of 1.0 m for the Forest Creek fault at the surface. It is important to note that the position of the scarp on the steep hillslope may complicate the relationship between surface slip and slip on the fault at depth (Khajavi *et al.*, 2014).

Because of the large uncertainties in the ages of earthquakes, an RI can only be estimated from the constraining ages of earthquakes in the trench. The maximum time interval between FC2 and FC3 is 5000 years; the minimum is 0 year. Placing the ages of the earthquakes at the centers of the age distributions for FC2 (~4.5 ka B.P.) and FC3 (2.5 ka B.P.) yields an RI of ~2000 years. Skewing the distributions based on our interpretations of the geology and rates of soil-forming processes (see above) lengthens this preliminary estimate of RI toward 3000 years.

Synthesis of Paleoseismic Data for the Fox Peak and Forest Creek Faults

Syntheses of paleoseismic trench results are presented in Table 2 and Figure 10. The ages of paleoseismic events were determined from five trenches on three faults/fault segments: the Cloudy Peaks and Bray segments of the Fox Peak fault and the northern segment of the Forest Creek fault. The age of one earthquake was constrained by dating displaced river terraces near the Bray–Cloudy Peaks segment boundary at the South Opuha River. These investigations have revealed the ages of three to four Fox Peak fault and three Forest Creek fault earthquakes, with varying degrees of aleatory and epistemic uncertainties. We present preferred age distributions for these earthquakes (Table 2; Fig. 10) based on uncertainty in the geochronologic data constraining the event timing and geologic observations.

Exponential distributions were used where either event age maxima or minima were constrained by geochronology, and the probability was inferred to decay away from this upper bound. For example, we consider the likely age of earthquake CP3 from trench 3 to be close to that of the calibrated age of 2513 ± 167 yr B.P., which is a maximum for the age of that event. Thus, the probability that the event is younger falls off exponentially toward an age of 0 years. Normal distributions were used where the earthquake age could be approximated by a preferred central value (mean) and uncertainty about that value.

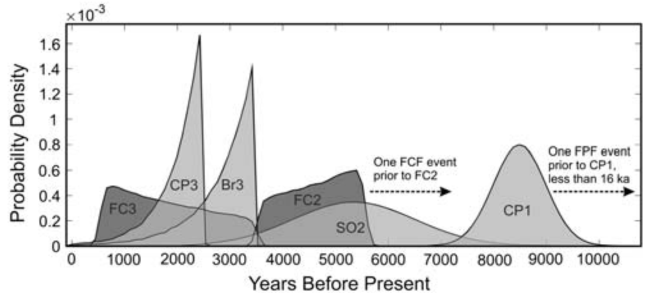

Figure 10. Probability density functions (PDFs) of event ages from paleoseismic trenching of the Fox Peak (light gray, FPF) and Forest Creek (dark gray, FCF) faults. The shapes of some distributions were specified *a priori* to incorporate geologic observations and constraining ages. FC3: most recent event (MRE) in trench 5 (Forest Creek fault) as an exponential function decreasing from ~500 yr B.P. to a cutoff value of 3500 yr B.P.; CP3, MRE in trench 3 (Fox Peak fault at Cloudy Peaks) as an exponential function decreasing from a maximum probability (oldest possible age of the earthquake) of ~2500 yr B.P.; Br3, MRE in trench 4 (Fox Peak fault at Fox Peak ski field road, Bray segment) as an exponential function decreasing from a maximum at its oldest age of 3500 yr B.P.; SO2, Penultimate Fox Peak fault event at the South Opuha River terraces, inferred from terrace ages as a normal distribution with 2σ constrained by upper and lower 95th percentiles for bounding terrace ages; FC2, Penultimate Forest Creek fault event as an exponential function decreasing from ~5500 to ~3500; CP1, preferred age of the antepenultimate event at Cloudy Peaks (trenches 1 and 2). A standard deviation of 500 years was used for CP1 (despite the actual uncertainty being smaller) to visualize all of the distributions on the same plot.

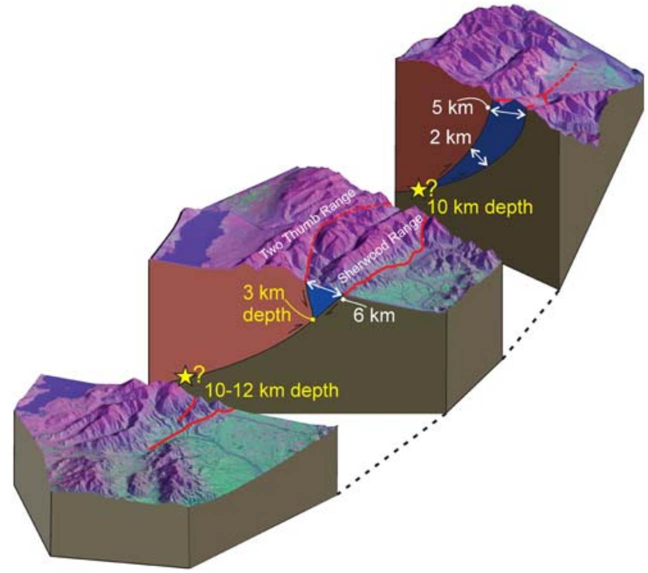

Figure 11. Landsat imagery and 15-m DEM block model of the field area. The Fox Peak fault (bounding the Sherwood Range) and Forest Creek fault (bounding the Two Thumb Range) are shown at the surface, with listric geometries predicted by regional geophysics studies, mapping, and modeling. Other faults, included in the cross section, have been mapped but do not have recent displacement and are not considered in this analysis. Stars show the typical hypocenter depths in the field area (middle section, see Fig. 13) and the branching depth of the listric Fox Peak and Forest Creek faults (northern section, top right). The color version of this figure is available only in the electronic edition.

Modeling Method

Because of the imprecision of the dating techniques, limited number of events, and uncertainty in timing of earthquake horizons between bounding strata, it cannot be determined absolutely whether overlapping age distributions represent coeval Fox Peak and Forest Creek fault earthquakes (Fig. 10). On a fast-slipping fault like the San Andreas, a stringing-pearls analysis like that conducted by Biasi and Weldon (2009) may be warranted to find the most appropriate rupture scenarios based on observations in many trenches. In this study, we calculate M_w and MCE for different rupture scenarios using a Monte Carlo simulation.

The M_w distribution for rupture on the Fox Peak and/or the Forest Creek faults depends on (1) the fault geometry and rupture area, (2) the input seismic parameters (e.g., shear modulus and displacement), and (3) the probability that rupture on one fault causes simultaneous rupture on the other. To address (1) and obtain the rupture area for (2), we combined field measurements of dip with constraints from regional studies (e.g., Wannamaker *et al.*, 2002; Long *et al.*, 2003; Upton *et al.*, 2004; Amos *et al.*, 2007; Beavan *et al.*, 2007) to interpolate fault surfaces and their areas (Fig. 11; Table 3). The varying structural models presented in these studies were analyzed to construct two credible geometries. The first geometry was constructed in Leapfrog Geo software (see Data and Resources) by specifying a surface dip of 55° for a listric Fox Peak fault that soles into a 15°–20° dipping ramp at ~4 km depth (after Long *et al.*, 2003; Amos *et al.*, 2007) near its southern tip. Surface measurements of dip and mapping further inform how the geometry of the Fox Peak fault changes along strike. The Forest Creek fault is inferred to sole into the Fox Peak fault, which is a consequence of it being antithetic to the Fox Peak fault in the south (T. Stahl *et al.*, unpublished manuscript; Long *et al.*, 2003; Fig. 11) and listric in the north (T. Stahl *et al.*, unpublished manuscript; Wannamaker *et al.*, 2002; Beavan *et al.*, 2007). For simplicity, the Forest Creek fault is modeled as one continuous structure that changes its vergence along strike, though it may be two distinct fault segments in actuality. The second geometry includes a planar, high-angle Fox Peak fault (55° dip) down to 5 km depth, flattening into a 30°-dipping planar fault and a 55°-dipping Forest Creek fault down to 12 ± 2 km depth, commensurate with steep dips on the fault through the seismogenic crust included in geodetic models and interpretations of magnetotelluric surveys (e.g., Beavan *et al.*, 2007). In both geometries, the fault width is cut off at 12 km (± 2 km for the planar geometry) depth, as defined by the base of the seismogenic zone for the region (e.g., Berryman *et al.*, 2002; Reyners *et al.*, 2011).

SEDs for the faults were measured from surveyed scarp profiles and fault exposures in trenches (T. Stahl *et al.*, unpublished manuscript; this study). Estimates of SED vary by location along faults segments and by the method used to derive them (T. Stahl *et al.*, unpublished manuscript). Individual measurements vary from 0.85 m at the South Opuha

Table 3
Input Parameters for Monte Carlo Simulation of M_w

	Input Parameter		
	Model Distribution	PDF Constraints	References
Shear modulus	Fixed	2.7×10^{11} dyn·cm^{-2}	Berryman *et al.* (2002)
Average SED	Trapezoidal	0.8-2-2.5-3 m*	Moss and Ross (2011), this study, and T. Stahl *et al.* (unpublished manuscript)
Subsurface:surface displacement ratio	Trapezoidal	1-1-4/3-5/3*	Berryman *et al.* (2002), Wesnousky (2008), this study, T. Stahl *et al.* (unpublished manuscript), and Wells and Coppersmith (1994)
FPF area (listric)	Fixed from model	2046 km^2	This study, T. Stahl *et al.* (unpublished manuscript), Long *et al.* (2003), Beavan *et al.* (2007), and Amos *et al.* (2007)
FCF area (listric)	Fixed from model	585 km^2	This study, T. Stahl *et al.* (unpublished manuscript), and Long *et al.* (2003)
Jump distance	Normal	2.5 ($\pm$ 2.5) km†	Shaw and Dieterich (2007), Long *et al.* (2003), Beavan *et al.* (2007), and Wannamaker *et al.* (2002)
R_0	Fixed	3‡	Shaw and Dieterich (2007) and Field *et al.* (2013)
FPF surface length	Fixed	35.7 km	This study and T. Stahl *et al.* (unpublished manuscript)
FCF surface length	Fixed	0, 15, 40 km	This study and T. Stahl *et al.* (unpublished manuscript)
Subsurface:surface length ratio (planar fault model only)	Trapezoidal	1-1-4/3-5/3*	Berryman *et al.*(2002), Wesnousky (2008), and Wells and Coppersmith (1994)
Fault dip (planar fault model only)	Fixed	FPF: 55° @ 0-5 km; 30° @ 5-ST km; FCF: 55° @ 0-ST km	This study, T. Stahl *et al.* (unpublished manuscript), Long *et al.* (2003), and Beavan *et al.* (2007)
Seismogenic thickness (ST) (planar fault model only)	Normal	12 ($\pm$2) km†	Berryman *et al.* (2002)

PDF, probability density function; SED, single event displacement; FPF, Fox Peak fault; FCF, Forest Creek fault.
*Lower bound, mode 1; mode 2, upper bound given for trapezoidal distributions.
†Mean and (2σ) given for normal distributions.
‡Single value is given where a constant is used.

River, ~1.8 m at Cloudy Peaks trench 3, to over 3 m in places along the Bray segment. We used a trapezoidal distribution for average surface displacement with the minimum, maximum, and modal probability values determined by this range observed in the field (Table 3). We give the highest preference (i.e., probability) to the 2–2.5 m range (T. Stahl *et al.*, unpublished manuscript; Table 3). Average surface displacement was then converted into an average subsurface displacement (ASD) using historical earthquake data from Wells and Coppersmith (1994), Berryman *et al.* (2002), and Wesnousky (2008) (Table 3; Fig. 12). We consider the range of ASD to surface displacement ratio to lie between 1 and 5/3 (Table 3 and references therein), though we are aware of some instances where the ratio can be outside this range. It is assumed in our models that the entirety of both fault planes are capable of storing elastic strain and rupturing, therefore contributing to the total seismic moment in large earthquakes. Shear modulus was fixed at 2.7×10^{11} dyn·cm^{-2} (Berryman *et al.*, 2002).

The exponential, distance-based jumping probability of Shaw and Dieterich (2007) is used to quantify the probability that ruptures on one fault causes simultaneous rupture on the other. We argue that this equation, developed from a numerical model of strike-slip faults, is considered reasonable for use in reverse faulting because reverse faults are historically more likely than strike-slip faults to jump segments (Field *et al.*, 2013), and this procedure allows specification of a jump distance based on constraints of subsurface geometry. Additionally, this model is easy to implement, agrees reasonably well with empirical datasets (e.g., Field *et al.*, 2013), and does not rely on interpretation of the mode of fault triggering (e.g., rupture branching, or static or dynamic triggering). For short distances (less than 10 km) the relationship is

$$p(r) = \exp\left(\frac{-r}{r_0}\right), \quad (1)$$

in which r is the jump distance, r_0 is a constant inversely proportional to the fall-off of probability with distance, and $p(r)$ is the jump probability (Shaw and Dieterich, 2007). We use a value of $r_0 = 3$, because this yields conservative probabilities of rupture jumping at $r \geq 5$ km that are consistent with the limited data for continental reverse-fault earthquakes (e.g., Rubin, 1996; Wesnousky, 2008; Field *et al.*, 2013).

A Monte Carlo simulation was used in which input parameters were allowed to vary based on uncertainties in the fault geometry, location on the Fox Peak fault where jumping occurs, and ASD (Fig. 12). In each iteration (i.e., earthquake), rupture on the Fox Peak fault jumps onto a length of the Forest Creek fault, depending on the randomly sampled r and exponential jump probability density function. M_w is then calculated from the cumulative rupture area, ASD, shear modulus, and relationship with seismic moment (Hanks and Kanamori, 1979).

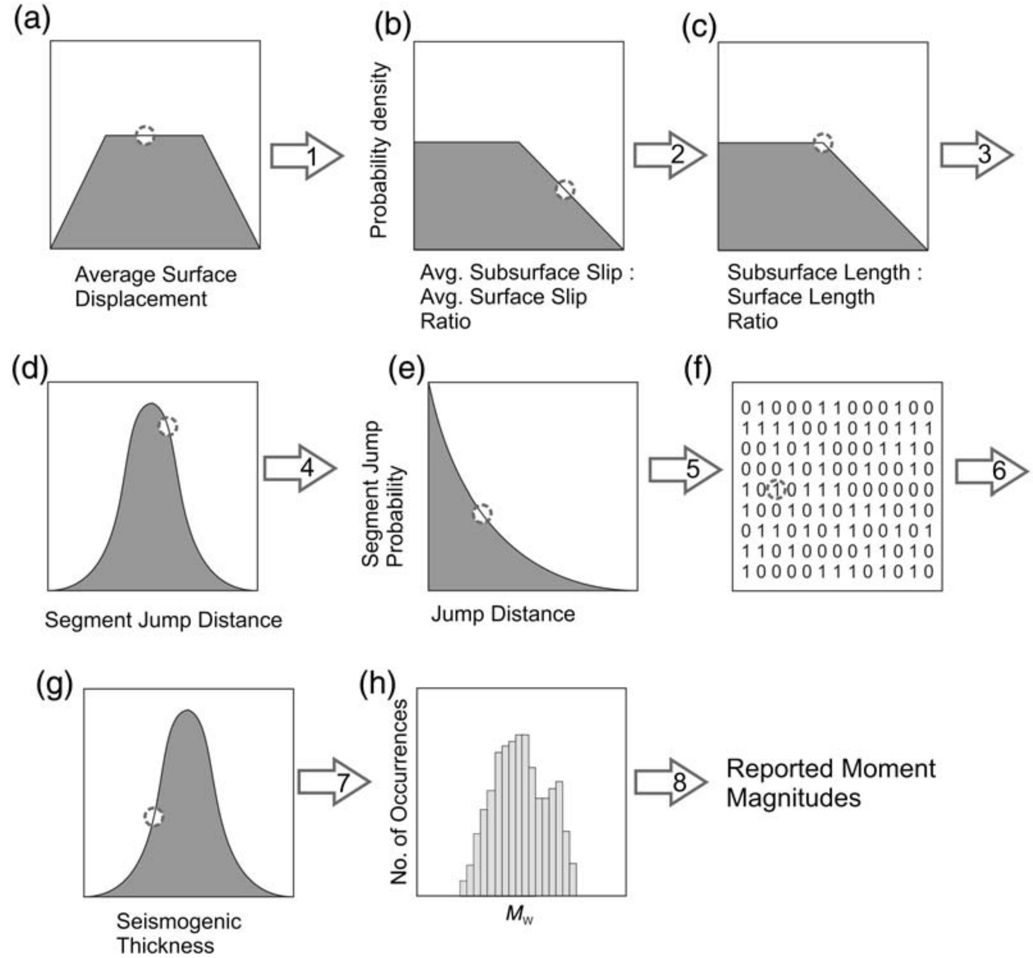

Figure 12. Algorithm for calculating M_w in the planar fault model. For each probability distribution, the values used can be found in Table 3. Dashed circles are examples of random samples from the allocated distribution. (a) Sample from an appropriate trapezoidal distribution to determine the average surface displacement. (b) Convert this average surface displacement into a subsurface displacement by randomly sampling an appropriate distribution for the ratio. (c) Perform the same sampling technique for converting surface length to subsurface length. (d) Sample from a normal distribution of step-over distances, which depends on how and where on the fault planes rupture initiates and propagates. Distance is not allowed to be negative. (e) Using the distance in (d), calculate the probability that rupture initiates on the Forest Creek fault. (f) Generate an array of ones and zeroes, in which 1 is that the Forest Creek fault ruptures and 0 is that the Forest Creek fault does not rupture, and the number of each in the matrix depends on value in (e). (g) Sample from the seismogenic thickness distribution. Step 7 uses the information from (a) to (g) to calculate the fault width, area, seismic moment, and finally M_w, using the equation of Hanks and Kanamori (1979) (see Table 3 for parameters). The process is repeated to produce (h). For the listric fault model M_w, the fault geometry is prespecified, so it only relies on (a), (b), (d), (e), and (f).

Coulomb stress modeling was used as a plausibility filter for our rupture models and conducted in Coulomb 3.3 (Lin and Stein, 2004). We consider three simple scenarios, each involving stress transfer from a rupturing Fox Peak fault onto the Forest Creek fault segments. The alternative (i.e., Forest Creek fault rupture triggering a Fox Peak fault rupture) was also considered; however, preliminary models suggest that the stress change induced by Forest Creek rupture on the Fox Peak fault is negligible. Static stress interactions between individual segments of Forest Creek fault and dynamic stress changes were not investigated.

For modeling in Coulomb 3.3, listric geometries for the Fox Peak and Forest Creek faults were constructed via connecting planar segments of different dips. The first considers 3 m of slip on the entirety of the Fox Peak fault, constructed from five segments that decrease in dip by 10° from 60° at the surface to 20° at 8–12 km depth. The second considers 3 m of slip only on the 20° dipping ramp at 8–12 km depth, where hypocenters cluster in the field area (Fig. 13). The third considers only 60° dipping planar faults with 3 m of slip on the Fox Peak fault tapering from the center of the fault. In each scenario, the receiver fault (Forest Creek fault) is subdivided into 3–4 km long and wide divisions. Coulomb stress was calculated for dip-slip motion on the Forest Creek and Fox Peak faults. We used a coefficient of friction of 0.8 (after Lin and Stein, 2004). We used default values of 8×10^5 bar for Young's modulus and 0.25 Poisson's ratio.

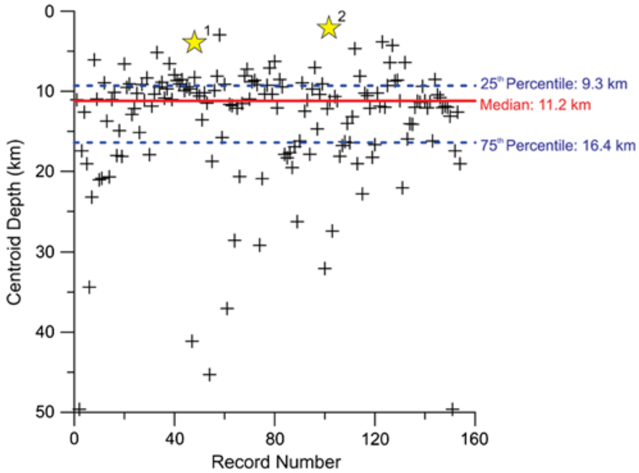

Figure 13. Relocated hypocenters for the central South Island (after Reyners *et al.*, 2011). Stars represent the depths of known, high-angle reverse-mechanism earthquakes: (1) indicates 2011 M_w 4.2 earthquake near the Ostler fault (data available from U.S. Geological Survey [USGS] (see Data and Resources) at 4 km depth; (2) indicates 2004 M_w 4.5 earthquake near the Fox Peak fault (data available from GeoNet, see Data and Resources) autolocated at 2 km depth. The color version of this figure is available only in the electronic edition.

Results

Five rupture scenarios are considered in the fault-triggering model (Fig. 14). The scenarios vary based on different allowable lengths and widths of the rupture on the faults. Variability about a peak (Fig. 14a) is due to uncertainty in the input parameters and consequent variability in each iteration of the model ($n = 25{,}000$ iterations). The shape of the output distribution in Figure 15a is determined by the input distributions and how often an earthquake is triggered on a specified length of the Forest Creek fault.

The M_w of an earthquake involving only the Fox Peak fault depends strongly on whether the fault is listric. The planar fault model produces an average of $M_w\,7.15^{+0.16}_{-0.19}$ (5th and 95th percentiles), which is consistent with the estimate in the National Seismic Hazard Model (NSHM) (Stirling *et al.*, 2012; M_w 7.2) and from the scaling laws presented in Moss and Ross (2011) and Wesnousky (2008) ($M_w\,7.03 \pm 0.24$ and 7.2 ± 0.3, respectively) (Fig. 14a, distribution [i]). Including a 15-km Forest Creek fault in the planar model increases the mean M_w and skews the distribution to the left ($M_w\,7.18^{+0.17}_{-0.22}$), but there is no distinguishable second mode in the data due to Forest Creek fault rupture (Fig. 14a, distribution [ii]). Inclusion of a 40-km Forest Creek fault results in a broader distribution with peaks at $M_w \sim 7.2$ and 7.30, though the summed effect of the uncertainty surrounding each peak results in an approximately trapezoidal distribution with an average of $M_w\,7.22^{+0.21}_{-0.23}$ (Fig. 14a, distribution [iii]).

The listric model distribution for the Fox Peak fault alone (Fig. 14a, distribution [iv]) produces an average of $M_w\,7.39^{+0.12}_{-0.15}$. The listric model produces an average of $M_w\,7.42^{+0.14}_{-0.16}$ for the 40-km Forest Creek fault rupture scenario (Fig. 14a, distribution [v]).

Cumulative distribution functions define the likely MCE for the Fox Peak and Forest Creek faults. We used the upper quartile of distributions (iv) and (v) to estimate an MCE of M_w 7.5–7.6 (Fig. 14b). It is noted that the uncertainty in the maximum M_w (the likely magnitudes of surface-rupturing earthquakes, given the different rupture scenarios) over the RI considered in this study (~2.5–3.5 ka) are better represented by the distributions themselves and range from $M_w \sim 7.1$ to 7.4.

The coulomb stresses induced on the Forest Creek fault by slip on the Fox Peak fault depend on the fault geometry used and the displacement pattern. For rupture on a moderately dipping (40°) reverse-fault plane (Fig. 15a), large positive changes (> 10 bar) are only induced on the lowest portion of the Forest Creek fault (10–12 km depth). Although this area is small compared to the total area of the fault, it coincides with the depth of hypocenters on the region (Fig. 13) and the nucleation depth for several historical $M_w > 7$ earthquakes in New Zealand's South Island (Doser *et al.*, 1999; Beavan *et al.*, 2012). Large stress shadows are located at the edges of the fault, and stress decreases on the southern Forest Creek fault are negligible.

For rupture on the gently dipping ramp of the Fox Peak fault (Fig. 15b), coulomb stresses show large (> 10 bar) increases on the 50°-dipping portion of the Fox Peak fault, the northern Forest Creek fault, and part of the southern Forest Creek fault. Stress increases on the northern Forest Creek fault coincide with the down-dip projection from the recent surface trace. Stress shadows in the middle section of the fault coincide with a lack of any observable Forest Creek fault trace at the up-dip projection of the fault (i.e., the surface) (T. Stahl *et al.*, unpublished manuscript). The steeply dipping planar fault model (Fig. 15c) shows large increases on the Forest Creek fault, except in the section that roughly coincides with the recent surface trace. Tapering of fault slip produces the same pattern of increases and decreases as nontapered slip.

Discussion

Evaluation of Monte Carlo Method

The Monte Carlo simulation in this study is different than logic-tree approaches in that the most likely jump distances and equation governing the jump probability are prespecified (equation 1), but the jump probabilities themselves are not user-specified. Thus, from iteration to iteration, the probability differs, depending on the particular rupture and the geometry of faulting. In this way, a range of probabilities tailored to the faults are expressed in the results, giving a better estimate of the inherent variability and uncertainty. Because the jump equation used in this study is dependent on fault-to-fault distance, many rupture scenarios, perhaps involving other faults, could be possible, though at large distances they become increasingly improbable (e.g., Parsons

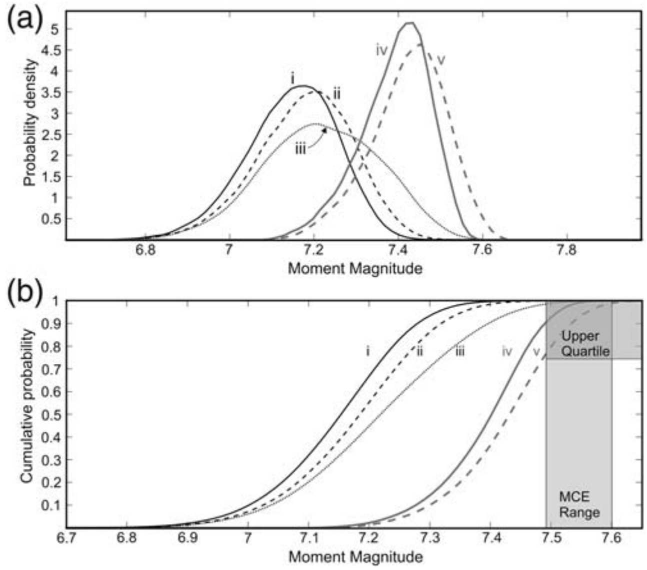

Figure 14. (a) PDFs of maximum M_w for five rupture scenarios, smoothed from output histograms using a normal kernel and bin width of 0.01. Planar fault models: (i) Fox Peak fault in isolation, (ii) Fox Peak fault allowing for 15-km surface length of Forest Creek fault, (iii) Fox Peak fault allowing for 40-km surface length of Forest Creek fault; listric fault models: (iv) Fox Peak fault in isolation, and (v) Fox Peak fault allowing for 40-km surface length of Forest Creek fault. (b) Corresponding cumulative distributions, showing how the MCE is calculated at the upper quartile of the moment magnitude distribution. See above text for discussion.

et al., 2012). We note that, should variable ranges (in the case of r_0 in equation 1) or more appropriate equations governing jump probability be determined, these can be easily implemented in Monte Carlo simulation. Furthermore, because fault kinematics and geometry are constrained in the present study, coulomb stress models can be used to test the feasibility of triggered slip. In other models, distributions of induced coulomb and dynamic stresses on a receiver fault plane could be used to calculate the jump probability directly, similar to cellular automata or synthetic seismicity models (e.g., Bebbington and Harte, 2003; Robinson, 2004).

Determination of Appropriate M_w Distributions for the Fox Peak and Forest Creek Faults

Distributions (i) (planar Fox Peak fault) and (iv) (listric Fox Peak fault) in Figure 15 represent calculations of M_w for an isolated rupture of the Fox Peak fault. Although distribution (i) agrees well with previous calculations, (iv) is ~1.5–2 times larger in terms of moment release. Because there is uncertainty in the depth and to which angle the Fox Peak fault flattens, it is difficult to favor one model over another for hazard purposes. The inclusion of variable Forest Creek fault rupture lengths in distribution (ii) (15-km Forest Creek fault rupture) and (iii) (40-km Forest Creek fault rupture) brings the average M_w closer to those derived in the listric fault models (iv) and (v). Estimates of M_w for a combined Fox Peak fault and Forest Creek fault rupture are significantly larger than that of a planar Fox Peak fault rupturing in isolation.

Coulomb stress modeling can assist with determining which rupture lengths of the Forest Creek fault are most likely when induced by slip on the Fox Peak fault (Fig. 15). This is not to imply that large patches of fault elements that see a stress increase will definitely rupture or that stress shadows on the fault planes are likely to act as barriers to rupture propagation. The length of the Forest Creek fault rupture, if any, is likely to depend strongly on the distribution of stress on the plane prior to the initiating earthquake (e.g., Steacy and McCloskey, 1998; Schwartz *et al.*, 2012) and dynamic stresses (Oglesby *et al.*, 2003). Additionally, triggering may take days to years, even if the faults have been partially synchronized over several earthquake cycles (Scholz, 2010). Coulomb calculations also assume crustal elasticity between source and receiver faults. A highly fractured intervening rock mass would affect the interpretation of our Coulomb model results.

Nonetheless, the minimum stress increases on parts of the Forest Creek fault in all Coulomb models (> 10 bar) are within the bounds of historical earthquake stress drops (e.g., Ruff, 1999; Baltay *et al.*, 2011) and suggest that our hypothesis of combined Fox Peak and Forest Creek ruptures represents a realistic scenario. Because this is in part an investigation of the MCE of the fault system, it is assumed that the Forest Creek fault is capable of being triggered at any point in its own earthquake cycle.

Caskey and Wesnousky (1997) found that sites of coulomb stress increases on one fault rupture coincided with the locations of surface rupture on another during the Fairview Peak and Dixie Valley earthquakes. Oglesby *et al.* (2003) found that coulomb stresses can predict, or even underpredict, the ability of ruptures to jump onto overlapping thrust faults. If this is true for the Fox Peak–Forest Creek fault system, then the stress increases observed on the northern Forest Creek fault underlying the recent surface trace at seismogenic depths may indicate that only this ~15 km stretch of fault consistently ruptures with the Fox Peak fault (Fig. 15a–c), and preference should be given to distribution (ii) in Figure 14. The overlap in the last two event ages on the faults is in agreement with this interpretation, though no paleoseismic data are available on the southern Forest Creek fault. The southern Forest Creek fault has variable stress increases/decreases, depending on the fault geometry used and location of slip on the Fox Peak fault (Fig. 15). Thus, the rupture length of the Forest Creek fault may also change based on the slip distribution on the Fox Peak fault in any given earthquake. For the purposes of seismic hazard, M_w distribution (iii) may be the most appropriate, as it accounts for the full-length Forest Creek fault rupture and it is consistent with the M_w of isolated Fox Peak fault ruptures as well.

Not surprisingly, the listric models have significantly larger fault widths and therefore larger M_w. If the listric geometry predicted by regional seismic surveys and fold models (Long *et al.*, 2003; Amos *et al.*, 2007) is correct, then

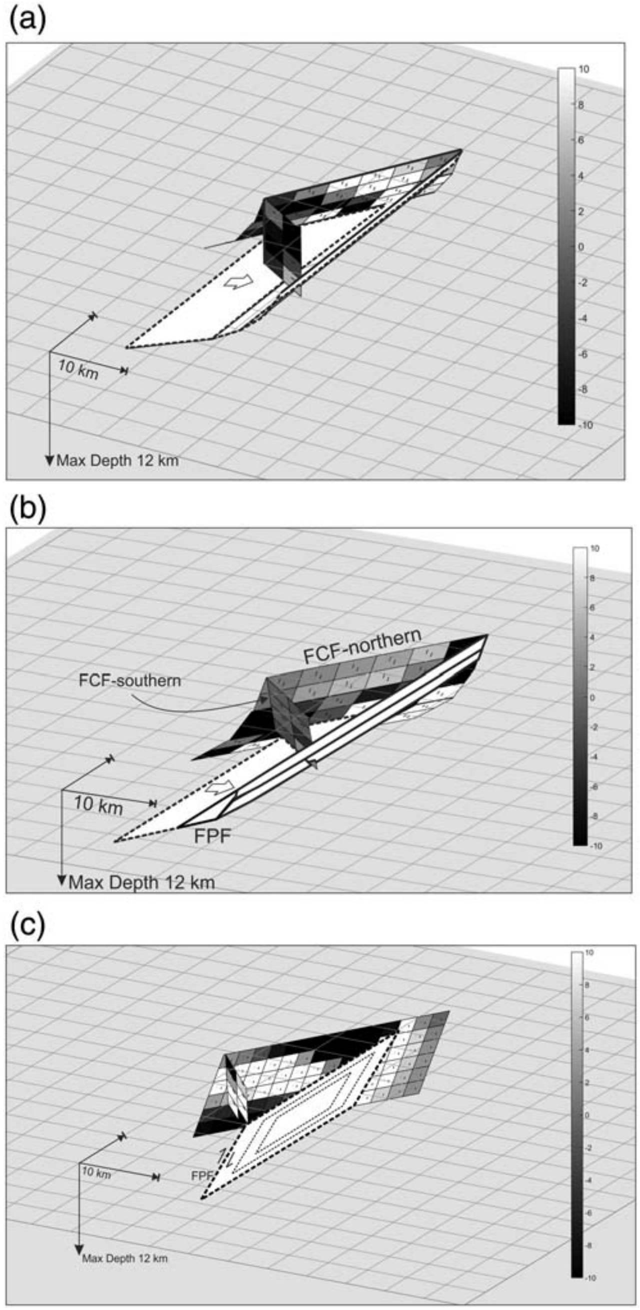

Figure 15. Induced coulomb stresses on the Forest Creek fault from rupture on the Fox Peak fault. (a) 3 m slip on all down-dip segments of the Fox Peak fault causes small decreases on the southern (antithetic) Forest Creek fault (~1 bar), small increases on the central Forest Creek fault (~2 bar), and large increases (> 10 bar) on the northern Forest Creek fault at depth. (b) 3 m slip on a 20°-dipping segment of the Fox Peak fault causes equal negative and positive changes on the southern Forest Creek fault, negative changes on the central Forest Creek fault (~3 bar), and large increases on the northern Forest Creek fault (5 bar). (c) 3 m tapered slip on the entirety of a steep (60° dipping Fox Peak fault) causes large increases on the southern Forest Creek fault (> 10 bar), large increases on most of the central and northern Forest Creek fault (> 10 bar), and a patch of large negative changes (< 10 bar) in the north.

the resultant increase in seismic moment outweighs the consideration of fault triggering in this study. Given that at least one historical earthquake has occurred on a listric reverse fault with no surface manifestation of a low-angle ramp (i.e., 2008 M_w 7.9 Wenchuan earthquake: Yu *et al.*, 2010; Zhang *et al.*, 2010), this requires serious attention in considering M_w calculations and determination of M_w and MCE. Given the modeling results and our field data, an M_w of 7.4 for the Fox Peak fault and an MCE of 7.5–7.6 (Fig. 14b) for both faults should be considered. These estimates greatly exceed the M_w of 7.2 that is currently used in the NSHM for the Fox Peak fault (the Forest Creek fault is not currently included in the NSHM, despite inclusion in New Zealand's active fault model; Litchfield *et al.*, 2014).

Conclusions

Multisegment and imbricate reverse-fault earthquakes pose a challenge to earthquake hazard models. Inability to quantitatively characterize a range of potential M_w and MCEs involving coeval rupture of linked faults can lead to large underestimates of hazard for a fault system (e.g., Parsons *et al.*, 2012; Field *et al.*, 2013; Hubbard *et al.*, 2014; DuRoss and Hylland, 2015). We obtained new paleoseismic data in five trenches from the Fox Peak and Forest Creek faults in the South Island, New Zealand. The data show MRE (~2500 yr B.P.) and penultimate event ages (~5000 yr B.P.) on the two faults that are consistent with, but not uniquely diagnostic of, coeval rupture of this imbricate fault system. Using the field data obtained in this study, as well as existing geophysical data, we provide a methodology for calculating M_w distributions and the MCE for this system of imbricate faults. The shape of M_w probability distributions for the Fox Peak and Forest Creek faults reflect the relative probabilities of isolated and triggered ruptures of the fault system. The results also indicate that earthquakes that rupture listric fault planes have the potential to produce significantly larger earthquakes (M_w 0.2–0.5 larger in our case study) than those on high-angle planar faults, due to the increased fault rupture area. Studies that do not take into account fault triggering or listric geometries could significantly underpredict the M_w and MCE of earthquakes.

Data and Resources

Earthquake data from GeoNet can be obtained at http://quakesearch.geonet.org.nz/ (last accessed March 2014); earthquake data from U.S. Geological Survey (USGS) can be searched at http://earthquake.usgs.gov/earthquakes/search/ (last accessed March 2014). Coulomb 3 software is available for download at http://earthquake.usgs.gov/research/software/coulomb/ (last accessed September 2013). Structural modeling and calculation of fault areas were conducted in ARANZ Geo Leapfrog Geo software. The unpublished manuscript "Tectonic geomorphology of the Fox Peak and Forest Creek faults, South Canterbury, New Zealand: Segmentation, slip rates, and earthquake magnitudes" by T. Stahl, M. Quigley, and M. Bebbington was accepted by *New Zeal. J. Geol. Geophys*.

Acknowledgments

This work was funded by New Zealand Earthquake Commission and University of Canterbury Mason Trust grants. Stahl was partially supported by a Canterbury International Doctoral Scholarship and by National Science Foundation (NSF) EAR Postdoctoral Fellowship Grant EAR-1451466. Reviews by Chris DuRoss and Glenn Biasi improved the quality of this article. We would like to thank Simon Brocklehurst, Stefan Winkler, and Jarg Pettinga for useful discussion surrounding trench interpretation and modeling methods. The assistance of Tom Brookman, Sam McColl, Travis Horton, Duncan Noble, Narges Khajavi, and Sharon Hornblow was invaluable in the field.

References

Alloway, B. V., D. J. Lowe, D. J. A. Barrell, R. M. Newnham, P. C. Almond, P. C. Augustinus, N. A. N. Bertler, L. Carter, N. J. Litchfield, M. S. McGlone, *et al.* (2007). Towards a climate event stratigraphy for New Zealand over the past 30,000 years (NZ-INTIMATE project), *J. Quaternary Sci.* **22,** 9–35.

Amos, C. B., D. W. Burbank, D. C. Nobes, and S. A. L. Read (2007). Geomorphic constraints on listric thrust faulting: Implications for active deformation in the Mackenzie basin, South Island, New Zealand, *J. Geophys. Res.* **112,** no. B03S11, doi: 10.1029/2006JB004291.

Amos, C. B., J. J. Lapwood, D. C. Nobes, D. W. Burbank, U. Rieser, and A. Wade (2011). Palaeoseismic constraints on Holocene surface ruptures along the Ostler fault, southern New Zealand, *New Zeal. J. Geol. Geophys.* **54,** 367–378.

Arrowsmith, J. R., C. J. Crosby, A. M. Korjenkov, E. Mamyrov, and I. E. Povolotskaya (2005). Surface rupture of the 1911 Kebin (Chon-Kemin) earthquake, Northern Tien Shan, Kyrgyzstan, *AGU* **86,** Fall Meet. Suppl., Abstract T51F-05.

Baltay, A., S. Ide, G. Prieto, and G. Beroza (2011). Variability in earthquake stress drop and apparent stress, *Geophys. Res. Lett.* **38,** no. 6, L06303, doi: 10.1029/2011GL046698.

Beavan, J., and J. Haines (2001). Contemporary horizontal velocity and strain rate fields of the Pacific-Australian plate boundary zone through New Zealand, *J. Geophys. Res.* **106,** 741–770.

Beavan, J., S. Ellis, and L. Wallace (2007). Kinematic constraints from GPS on oblique convergence of the Pacific and Australian plates, central South Island, New Zealand, in *A Continental Plate Boundary: Tectonics at South Island, New Zealand*, D. A. Okaya, T. A. Stern, and F. J. Davey (Editors), American Geophysical Union, Washington, D.C., 369 pp.

Beavan, J., M. Motagh, E. J. Fielding, N. Donnelly, and D. Collett (2012). Fault slip models of the 2010–2011 Canterbury, New Zealand, earthquakes from geodetic data and observations of postseismic ground deformation, *New Zeal. J. Geol. Geophys.* **55,** 207–221.

Bebbington, M., and D. Harte (2003). The linked stress release model for spatio-temporal seismicity: Formulations, procedures and applications, *Geophys. J. Int.* **154,** no. 3, 925–946.

Berryman, K. R., T. Webb, N. Hill, M. Stirling, D. J. Rhoades, J. Beavan, and D. Darby (2002). Seismic loads on Dams, Waitaki system: Earthquake source characterization, *GNS Client Rept. 2001/129*, 80 pp.

Biasi, G. P., and R. J. Weldon (2009). San Andreas fault rupture scenarios from multiple paleoseismic records: Stringing pearls, *Bull. Seismol. Soc. Am.* **99,** 471–498.

Carpenter, N. S., S. J. Payne, and A. L. Schafer (2012). Toward reconciling magnitude discrepancies estimated from paleoearthquake data, *Seismol. Res. Lett.* **83,** 555–565.

Caskey, S. J., and S. G. Wesnousky (1997). Static stress changes and earthquake triggering during the 1954 Fairview Peak and Dixie Valley earthquakes, central Nevada, *Bull. Seismol. Soc. Am.* **87,** no. 3, 521–527.

Cox, S. C., and D. J. A. Barrell (2007). Geology of the Aoraki area, *GNS Science. Institute of Geological & Nuclear Sciences Geological Map 15*, Lower Hutt, New Zealand, scale 1:250,000, 1 sheet, 71 pp.

DeMets, C., R. G. Gordon, and D. F. Argus (2010). Geologically current plate motions, *Geophys. J. Int.* **181,** 1–80.

Densmore, A. L., Y. Li, N. J. Richardson, R. J. Zhou, M. Ellis, and Y. Zhang (2010). The role of late quaternary upper-crustal faults in the 12 May 2008 Wenchuan earthquake, *Bull. Seismol. Soc. Am.* **100,** 2700–2712.

dePolo, C. M., and D. B. Slemmons (1990). Estimation of earthquake size for seismic hazards, in *Neotectonics and Earthquake Evaluation*, E. L. Krinitsky and D. B. Slemmons (Editors), Vol. 8, Reviews in Engineering Geology, Geological Society of America, 1–28.

Dolan, J. F., K. Sieh, T. K. Rockwell, R. S. Yeats, J. Shaw, J. Suppe, G. J. Huftile, and E. M. Gath (1995). Prospects for larger or more frequent earthquakes in the Los Angeles metropolitan region, *Science* **267,** 199.

Doser, D. I., T. H. Webb, and D. E. Maunder (1999). Source parameters of large historical (1918–962) earthquakes, South Island, New Zealand, *Geophys. J. Int.* **139,** no. 3, 769–794.

DuRoss, C. B., and M. D. Hylland (2015). Synchronous ruptures along a major graben-forming fault system: Wasatch and West valley fault zones, Utah, *Bull. Seismol. Soc. Am.* **105,** no. 1, 14–37.

Elliott, A., J. F. Dolan, and D. D. Oglesby (2009). Evidence from coseismic slip gradients for dynamic control on rupture propagation and arrest through stepovers, *J. Geophys. Res.* **114,** no. B02313, doi: 10.1029/2008JB005969.

Elliott, J. R., E. K. Nissen, P. C. England, J. A. Jackson, S. Lamb, Z. Li, M. Oehlers, and B. Parsons (2012). Slip in the 2010–2011 Canterbury earthquakes, New Zealand, *J. Geophys. Res.* **117,** no. B03401, doi: 10.1029/2011JB008868.

Field, E. H., and M. T. Page (2011). Estimating earthquake-rupture rates on a fault or fault system, *Bull. Seismol. Soc. Am.* **101,** 79–92.

Field, E. H., G. P. Biasi, P. Bird, T. E. Dawson, K. R. Felzer, D. D. Jackson, K. M. Johnson, T. H. Jordan, C. Madden, A. J. Michael, *et al.* (2013). Uniform California earthquake rupture forecast, version 3 (UCERF3)—The time-independent model, *U.S. Geol. Surv. Open-File Rept. 2013–1165, California Geological Survey Special Report 228, and Southern California Earthquake Center Publication 1792*, 97 pp.

Fukuyama, E., and K. X. Hao (2013). Subparallel dipping faults that ruptured during the 2008 Wenchuan earthquake, *Bull. Seismol. Soc. Am.* **103,** 2128–2134.

Gold, R. D., E. Cowgill, X. F. Wang, and X. H. Chen (2006). Application of trishear fault-propagation folding to active reverse faults: Examples from the Dalong fault, Gansu province, NW China, *J. Struct. Geol.* **28,** 200–219.

Gonzalez, G., M. Gerbault, J. Martinod, J. Cembrano, D. Carrizo, R. Allmendinger, and J. Espina (2008). Crack formation on top of propagating reverse faults of the Chuculay fault system, northern Chile: Insights from field data and numerical modelling, *J. Struct. Geol.* **30,** 791–808.

Hanks, T. C., and H. Kanamori (1979). A moment magnitude scale, *J. Geophys. Res.* **84,** no. B5, 2348–2350.

Heddar, A., C. Authemayou, H. Djellit, A. K. Yelles, J. Déverchère, S. Gharbi, A. Boudiaf, and B. Van Vliet Lanoe (2013). Preliminary results of a paleoseismological analysis along the Sahel fault (Algeria): New evidence for historical seismic events, *Quaternary Int.* **302,** 210–223.

Hubbard, J., J. H. Shaw, J. Dolan, T. L. Pratt, L. McAuliffe, and T. K. Rockwell (2014). Structure and seismic hazard of the Ventura Avenue anticline and Ventura fault, California: Prospect for large, multisegment ruptures in the western Transverse Ranges, *Bull. Seismol. Soc. Am.* **104,** 1070–1087.

Jackson, J., R. Norris, and J. Youngson (1996). The structural evolution of active fault and fold systems in central Otago, New Zealand: Evidence revealed by drainage patterns, *J. Struct. Geol.* **18,** nos. 2/3, 217–234.

Khajavi, N., M. C. Quigley, and R. M. Langridge (2014). Influence of topography and basement depth on surface rupture morphology revealed from LiDAR and field mapping, Hope Fault, New Zealand, *Tectonophysics* **630,** 265–284.

Lin, J., and R. Stein (2004). Stress triggering in thrust and subduction earthquakes and stress interaction between the southern San Andreas and nearby thrust and strike-slip faults, *J. Geophys. Res.* **109,** no. B02303, doi: 10.1029/2003JB002607.

Litchfield, N. J., R. Van Dissen, R. Sutherland, P. M. Barnes, S. C. Cox, R. Norris, R. J. Beavan, R. Langridge, P. Villamor, K. Berryman, *et al.* (2014). A model of active faulting in New Zealand, *New Zeal. J. Geol. Geophys.* **57,** no. 1, 32–56.

Long, D. T., S. C. Cox, S. Bannister, M. C. Gerstenberger, and D. Okaya (2003). Upper crustal structure beneath the eastern Southern Alps and the Mackenzie basin, New Zealand, derived from seismic reflection data, *New Zeal. J. Geol. Geophys.* **46,** 21–39.

McCalpin, J. (2009). *Paleoseismology*, Academic Press, Burlington, Massachusetts, 613 pp.

McCormac, F. G., A. G. Hogg, P. G. Blackwell, C. E. Buck, T. F. G. Higham, and P. J. Reimer (2004). SHCal04 Southern Hemisphere Calibration, 0–11.0 cal kyr BP, *Radiocarbon* **46,** 1087–1092.

Moss, R. E. S., and Z. E. Ross (2011). Probabilistic fault displacement hazard analysis for reverse faults, *Bull. Seismol. Soc. Am.* **101,** no. 4, 1542–1553.

Oglesby, D. D., S. M. Day, and D. R. H. O'Connell (2003). Dynamic and static interaction of two thrust faults: A case study with general implications, *J. Geophys. Res.* **108,** no. B10, 2489.

Oskin, M. E., J. R. Arrowsmith, A. H. Corona, A. J. Elliott, J. M. Fletcher, E. J. Fielding, P. O. Gold, J. J. G. Garcia, K. W. Hudnut, J. Liu-Zeng, *et al.* (2012). Near-field deformation from the El Mayor–Cucapah earthquake revealed by differential LIDAR, *Science* **335,** 702–705.

Parsons, T., E. H. Field, M. T. Page, and K. Milner (2012). Possible earthquake rupture connections on mapped California faults ranked by calculated coulomb linking stresses, *Bull. Seismol. Soc. Am.* **102,** 2667–2676.

Reyners, M., D. Eberhart-Phillips, and S. Bannister (2011). Tracking repeated subduction of the Hikurangi plateau beneath New Zealand, *Earth Planet. Sci. Lett.* **311,** nos. 1/2, 165–171.

Robinson, R. (2004). Potential earthquake triggering in a complex fault network: The northern South Island, New Zealand, *Geophys. J. Int.* **159,** no. 2, 734–748.

Rubin, C. M. (1996). Systematic underestimation of earthquake magnitudes from large intracontinental reverse faults: Historical ruptures break across segment boundaries, *Geology* **24,** 989–992.

Ruff, L. J. (1999). Dynamic stress drop of recent earthquakes: Variations within subduction zones, *Pure Appl. Geophys.* **154,** 409–431.

Scholz, C. H. (2010). Large earthquake triggering, clustering, and the synchronization of faults, *Bull. Seismol. Soc. Am.* **100,** no. 3, 901–909.

Schwartz, D. P., P. J. Haeussler, G. G. Seitz, and T. E. Dawson (2012). Why the 2002 Denali fault rupture propagated onto the Totschunda fault: Implications for fault branching and seismic hazards, *J. Geophys. Res.* **117,** no. B11304, doi: 10.1029/2011JB008918.

Shaw, B. E., and J. H. Dieterich (2007). Probabilities for jumping fault segment stepovers, *Geophys. Res. Lett.* **34,** L01307, doi: 10.1029/2006gl027980.

Stahl, T., S. Winkler, M. Quigley, M. Bebbington, B. Duffy, and D. Duke (2013). Schmidt hammer exposure-age dating (SHD) of late quaternary fluvial terraces in New Zealand, *Earth Surf. Process. Landf.* **38,** no. 15, 1838–1850.

Steacy, S. J., and J. McCloskey (1998). What controls an earthquake's size? Results from a heterogeneous cellular automaton, *Geophys. J. Int.* **133,** no. 1, F11–F14.

Stirling, M. W., G. H. McVerry, and K. R. Berryman (2002). A new seismic hazard model for New Zealand, *Bull. Seismol. Soc. Am.* **92,** no. 5, 1878–1903.

Stirling, M. W., G. H. McVerry, M. Gerstenberger, N. Litchfield, R. Van Dissen, K. R. Berryman, P. M. Barnes, L. Wallace, P. Villamor, R. Langridge, *et al.* (2012). National seismic hazard model for New Zealand: 2010 update, *Bull. Seismol. Soc. Am.* **102,** no. 4, 1514–1542.

Tonkin, P. J., and L. R. Basher (1990). Soil-stratigraphic techniques in the study of soil and landform evolution across the Southern Alps, New Zealand, *Geomorphology* **3,** 547–575.

Upton, P., and E. C. Osterberg (2007). Paleoseismicity and mass movements interpreted from seismic-reflection data, Lake Tekapo, South Canterbury, New Zealand, *New Zeal. J. Geol. Geophys.* **50,** 343–356.

Upton, P., D. Craw, Z. James, and P. O. Koons (2004). Structure and late Cenozoic tectonics of the southern Two Thumb range, mid Canterbury, New Zealand, *New Zeal. J. Geol. Geophys.* **47,** 141–153.

Wallace, L. M., J. Beavan, R. McCaffrey, K. Berryman, and P. Denys (2007). Balancing the plate motion budget in the South Island, New Zealand using GPS, geological and seismological data, *Geophys. J. Int.* **168,** 332–352.

Wannamaker, P. E., G. R. Jiracek, J. A. Stodt, T. G. Caldwell, V. M. Gonzalez, J. D. McKnight, and A. D. Porter (2002). Fluid generation and pathways beneath an active compressional orogen, the New Zealand Southern Alps, inferred from magnetotelluric data, *J. Geophys. Res.* **107,** 2117.

Wells, D. L., and K. J. Coppersmith (1994). New empirical relationships among magnitude, rupture length, rupture width, rupture area, and surface displacement, *Bull. Seismol. Soc. Am.* **84,** no. 4, 974–1002.

Wesnousky, S. G. (2006). Predicting the endpoints of earthquake ruptures, *Nature* **444,** 358–360.

Wesnousky, S. G. (2008). Displacement and geometrical characteristics of earthquake surface ruptures: Issues and implications for seismic-hazard analysis and the process of earthquake rupture, *Bull. Seismol. Soc. Am.* **98,** 1609–1632.

Xu, X., X. Wen, G. Yu, G. Chen, Y. Klinger, J. Hubbard, and J. Shaw (2009). Coseismic reverse- and oblique-slip surface faulting generated by the 2008 M_w 7.9 Wenchuan earthquake, China, *Geology* **37,** 515–518.

Yu, G., T. Guo, X. Sun, X. Tan, Y. An, X. Xu, Y. Klinger, G. Diao, G. Chen, X. Feng, *et al.* (2010). Fault-scarp features and cascading-rupture model for the M_w 7.9 Wenchuan earthquake, eastern Tibetan plateau, China, *Bull. Seismol. Soc. Am.* **100,** no. 5B, 2590–2614.

Zhang, P. Z., X. Z. Wen, Z. K. Shen, and J. H. Chen (2010). Oblique, high-angle, listric-reverse faulting and associated development of strain: The Wenchuan earthquake of May 12, 2008, Sichuan, China, *Annu. Rev. Earth Planet. Sci.* **38,** no. 1, 353–382.

Zhu, S. B., and P. Z. Zhang (2010). Numeric modeling of the strain accumulation and release of the 2008 Wenchuan, Sichuan, China, earthquake, *Bull. Seismol. Soc. Am.* **100,** 2825–2839.

Department of Earth and Environmental Sciences
University of Michigan
1100 North University Avenue
Ann Arbor, Michigan 48109-1005
(T.S.)

School of Earth Sciences
The University of Melbourne
Parkville, Victoria 3010, Australia
(M.C.Q.)

Department of Geological Sciences
University of Canterbury
Private Bag 4800
Christchurch 8140, New Zealand
(A.M.)

Volcanic Risk Solutions
Massey University
Palmerston North 4442, New Zealand
(M.S.B.)

Manuscript received 14 August 2015;
Published Online 26 July 2016